

# The Transition ~~from-between~~ Supercooled Liquid Water ~~and to~~ Ice Crystals in Mixed-phase Clouds based on Airborne In-situ Observations

Flor Vanessa Maciel<sup>1,2</sup>, Minghui Diao<sup>1</sup>, Ching An Yang<sup>1</sup>

<sup>1</sup>Department of Meteorology and Climate Science, San Jose State University, San Jose, 95192, USA

<sup>2</sup>Current affiliation: Department of Atmospheric and Oceanic Sciences, University of California, Los Angeles, 90095, USA.

Correspondence to: Minghui Diao (minghui.diao@sjsu.edu)

**Abstract.** The on-set of ice nucleation in mixed-phase clouds determines ice cloud lifetime and their microphysical properties. In this work, we develop a novel method that differentiates ~~the early and later~~ various transition phases of mixed-phase clouds, ~~i.e., such as clouds dominated by pure liquid or pure ice segments, compared with those having~~ ice crystals ~~are initially~~ surrounded by supercooled liquid water droplets ~~or vice versa, then as they grow, pure ice segments are formed~~. Using this method, we examine the relationship between the macrophysical and microphysical properties of mixed-phase clouds. The results show that ~~evolution-the exchange between supercooled liquid water and ice crystals in a of cloud~~ macrophysical ~~properties~~ perspective, represented by the increasing spatial ratio of regions containing ice crystals relative to the total in-cloud region (defined as ice spatial ratio), is positively correlated with the ~~evolution-phase exchange of in a~~ microphysical ~~properties~~ perspective, represented by the increasing ice water content (IWC) and decreasing liquid water content (LWC). The mass partition transition from liquid to ice becomes more significant during ~~the later transition phase (i.e., transition phase 3)~~ when pure ice cloud regions (ICRs) start to appear. Occurrence frequencies of cloud thermodynamic phases show significant transition from liquid to ice at a similar temperature (i.e., -17.5°C) among three types of definitions of mixed-phase clouds based on ice mass fraction, ice number fraction, or ice spatial ratio. Aerosol indirect effects are quantified for different transition phases using number concentrations of aerosols greater than 100 nm or 500 nm ( $N_{>100}$  and  $N_{>500}$ , respectively).  $N_{>500}$  shows stronger positive correlations with ice spatial ratios compared with  $N_{>100}$ . This result indicates that larger aerosols potentially contain ice nucleating particles (INPs), which facilitate the formation of ice crystals in mixed-phase clouds. The impact of  $N_{>500}$  is also more significant ~~on-in the earlier~~ transition phase 2 when ice crystals just start to appear in mixed phase compared with ~~the later~~ transition phase 3 when pure ICRs have formed, possibly due to the competing aerosol indirect effects on primary and secondary ice production in phase 3. The thermodynamic and dynamic conditions are quantified for each transition phase. The results show in-cloud turbulence as a main mechanism for both the initiation of ice nucleation and the maintenance of supercooled liquid water, while ~~updrafts-large-scale ascent is~~ are important for the latter but not the former. Overall, these results illustrate the varying effects of aerosols, thermodynamics, and dynamics through ~~out~~ various stages of mixed-phase cloud evolution based on this new method that categorizes cloud transition phases.

Formatted: Superscript

Formatted: English (United Kingdom)

Formatted: Justified, Space Before: 6 pt, Don't add space between paragraphs of the same style

## 1 Introduction

Clouds with different thermodynamic phases can have contrasting influences on the net radiation at the top of atmosphere, depending on their microphysical properties, spatial extent and the distributions of hydrometeors (Matus and L'Ecuyer, 2017).

35 Among three types of cloud phases (i.e., ice, liquid, and mixed), mixed-phase clouds contain both supercooled liquid water and ice crystals. Radiative forcing of mixed-phase clouds over the Southern Ocean has large impacts on Earth's climate based on global climate model simulations (e.g., Tan et al., 2016; Hyder et al., 2018). Evaluating and improving the model parameterizations of mixed-phase clouds requires an improved understanding of their macrophysical and microphysical properties, as well as the factors controlling their formation and evolution.

40 Previous observations of mixed-phase clouds in the high latitudes have identified complex structures both vertically and horizontally. Using aircraft-based observations over the Southern Ocean, a high frequency of supercooled liquid water was found within low-level clouds in this region, and mixed-phase cloud segments were found to be more spatially heterogeneous compared with the pure liquid and pure ice segments (D'Alessandro et al., 2021). When calculating cloud top phase frequencies as a function of cloud top temperature by using aircraft-based lidar and radar observations over the Southern Ocean, liquid phase was seen as the dominant phase for 74.9% of the cloud top cases with subfreezing temperatures, and supercooled liquid water was found in cloud tops at temperatures as low as  $-30^{\circ}\text{C}$  (Zaremba et al., 2020). Using a large dataset collected by the Convair 580 aircraft of the National Research Council (NRC) of Canada it was found that several microphysical properties are dependent upon temperature, including supercooled liquid droplet concentration (Nliq), ~~ice and liquid water content (IWC,~~ and LWC, ~~respectively~~) (Korolev et al., 2003).

50 Ice nucleation within mixed-phase clouds and the factors behind the sustainability of mixed-phase clouds are still topics of contention within the field. The ~~resilience-persistent existence~~ of mixed-phase cloud systems ~~has~~ve been shown to be affected by local processes such as the formation and growth of cloud droplets and ice crystals (Morrison et al., 2012). The thermodynamics and dynamics of the atmosphere also play a large role in affecting the formation and development of mixed-phase clouds. Using observations of vertical motion within Arctic mixed-phase stratiform, Shupe et al. (2008) showed that an in-cloud updraft sustains the clouds, which also supports growth of ice and liquid mass concentrations. Their results also suggest that ice crystal concentrations (Nice) are often limited in order to support the persistent supercooled liquid water. 55 The connection between ice formation and vertical air velocity at cloud base was examined for mixed-phase clouds with less than 380-m depth by using ground-based Doppler lidar and cloud radar, and the mass flux of IWC was found to increase by two orders of magnitude when the vertical velocity fluctuation increases (Bühl et al., 2019). A study analyzed generating cells of ice crystals inside mixed-phase cloud layers over the Southern Ocean and found that these generating cells have small horizontal widths and contain supercooled liquid water with higher LWC and Nliq than that of the areas between the generating 60 cells, which also held true for ice particles whose dispersions, number concentration, and sizes are larger within the generating cells (Wang et al., 2020). With seven years of ground-based observations ~~at~~ an Alaskan site, it was found that Arctic mixed-

phase clouds occur less often in the early fall when the winds are southerly as the atmosphere is more stable, drier, colder and has lower relative humidity. Conversely, during northerly winds they have a wider particle distributions (Qiu et al., 2018).

65 Aerosols have been documented to influence the microphysical properties of mixed-phase clouds around the globe. Field study observations over a fourteen-year time period and from various locations around the Earth were combined to show that both temperature and the number concentration of aerosols larger than 0.5  $\mu\text{m}$  in diameter can impact the concentrations of growing INPs ice nuclei in mixed-phase clouds (DeMott et al., 2010). From aircraft observations over the Arctic, it was found that entrainment above mixed-phase clouds could enhance Nice and aerosol thermodynamic indirect effect likely occurs (Jackson et al., 2012). Using a nine-year long aerosol dataset, Norgren et al. (2018) found that clean mixed-phase clouds with a lower aerosols loading have a higher IWC at their base compared with clouds with a higher aerosol loading. Other studies over the Southern Ocean, e.g., McFarquhar et al. (2021), showed that those environments are primarily pristine, suggesting limited long-range continental aerosol transport and potentially more aerosols newly formed over the high southern latitudes. Observations and simulations of ice nucleating particles (INPs) showed that sea spray aerosol may play a major role to initiate primary ice nucleation in low-level mixed-phase clouds over the Southern Ocean (McCluskey et al., 2018). Besides primary ice production, secondary ice production has also been shown to be a critical process enhancing Nice in mixed-phase clouds based on both in-situ airborne observations (Huang et al., 2017; Järvinen et al., 2022) and global climate simulations (Zhao and Liu, 2021; Zhao et al., 2023) over the Southern Ocean. Secondary ice production can also be affected by aerosol loading, e.g., higher concentrations of cloud condensation nuclei can lead to higher supercooled liquid droplet concentrations, and therefore reducing the efficiency of the rime-splintering process.

80 These aforementioned studies demonstrated that the coexistence and interaction between supercooled liquid droplets and ice crystals hold a key for understanding the persistence of mixed-phase clouds despite of ice-liquid mixtures being unstable. An examination of aerosol indirect effects on liquid and ice hydrometeors separately is also a critical step towards a better understanding of the net aerosol indirect effects on the entire cloud (Korolev et al., 2017; Storelvmo, 2017). Targeting these topics, in this work, we develop a method to identify several transition phases of mixed-phase clouds, by using the spatial relationships between among segments containing only pure ice or only liquid, as well as those containing both ice and liquid. In section 2, a description of the observation dataset and instruments is given. In section 3, the details of the identification of four transition phases, their occurrence frequencies, and comparisons with previously established mixed-phase cloud definitions are provided. A contrast of thermodynamic and dynamic conditions among these transition phases is shown.

85 In addition, the relationships between macrophysical and microphysical properties of mixed-phase clouds during their evolution various transition phases are examined. Aerosol indirect effects from larger and smaller aerosols are quantified for individual transition phases, followed by a contrast of thermodynamic and dynamic conditions among these transition phases. Lastly, in section 4, we discuss the applications of this method for contrasting different definitions of mixed-phase clouds, and the implications of model parameterizations.

## 95 2 Observational Dataset

### 2.1 SOCRATES In-situ Observations and Instrumentation

The U.S. National Science Foundation (NSF) Southern Ocean Clouds, Radiation, Aerosol Transport Experimental Study (SOCRATES) flight campaign was conducted from January 15<sup>th</sup> to February 24<sup>th</sup> in 2018 (McFarquhar et al., 2021). This NSF-funded campaign utilized the NSF/National Center for Atmospheric Research (NCAR) Gulfstream V (G-V) research aircraft which flew over the Southern Ocean region of 62°S–42°S and 133°E–164°E as shown in Figure 1. A total of fifteen research flights (RFs) in this campaign were performed with a combined total of 111 flight hours flown. In this work, we applied a temperature restriction of –40°C to 0°C, commonly known as the mixed-phase cloud regime as this temperature range allows for the occurrence of both ice particles and supercooled liquid water, for all our analyses.

The NSF G-V research aircraft during the SOCRATES campaign was equipped with various scientific instruments to measure the various characteristics of the atmosphere, such as aerosol number concentrations (Na), cloud microphysical properties and common meteorological components – temperature, pressure, wind speed and humidity. The temperature was measured by the Rosemount temperature probe. To measure the water vapor molecule number density at 25-Hz resolution the Vertical Cavity Surface Emitting Laser (VCSEL) hygrometer was used. The final data reported the water vapor mixing ratio in 1-Hz resolution and a corrected version of water vapor data based on a post-campaign calibration in summer 2018 is used in this study (Diao, 2021). The water vapor and temperature data are used to calculate relative humidity with respect to liquid and ice (RH<sub>liq</sub> and RH<sub>i</sub>), by using the equations for saturation vapor pressure with respect to liquid and ice from Murphy and Koop (2005), respectively. The uncertainties associated with RH<sub>liq</sub> and RH<sub>i</sub> originate from both water vapor and temperature measurements, which sum up to 6%–7% for the mixed-phase cloud regime. We placed a ceiling on RH values by restricting all RH<sub>liq</sub> greater than 101% to 101%. The hydrometeor measurements used in this study were obtained from the Two-Dimensional Stereo Probe (2DS) and the cloud droplet probe (CDP), which have size ranges at 40 – 5000 μm and 2 – 50 μm, respectively. IWC and LWC are derived from 2DS and CDP probes following the method described in Yang et al. (2021).

That is, a mass-Dimension relationship based on a spherical shape is used to calculate LWC for liquid droplets in both CDP and 2DS measurements. A mass-Dimension relationship based on Wu and McFarquhar (2016) is used to calculate IWC for ice particles in 2DS measurements. In-cloud conditions are defined as the 1-Hz measurements with total water content (TWC = IWC+LWC) greater than 0.001 g m<sup>-3</sup>. Lower IWC and LWC values have also been reported by the two probes, but the threshold of 0.001 g m<sup>-3</sup> is chosen here due to the larger uncertainties of these cloud probes reporting lower mass concentrations of hydrometeors (e.g., Baumgardner et al., 2017). To provide a more focused analysis of cloud layers instead of precipitation below the clouds, we use two remote sensing instruments onboard the G-V aircraft – NSF/NCAR High-performance Instrumented Airborne Platform for Environmental Research (HIAPER) Cloud Radar (HCR) and High Spectral Resolution Lidar (HSRL) to identify potential precipitating samples. The particle identification (PID) product is used, which includes identifications of 11 categories – rain, supercooled rain, drizzle, supercooled drizzle, cloud liquid, supercooled cloud liquid, melting, large frozen, small frozen, precipitation and cloud (Romatschke and Vivekanandan, 2022). By manually inspecting

Formatted: Superscript

Formatted: Superscript

hourly time series of this product, we remove segments that are identified as precipitation, supercooled drizzle, drizzle, supercooled rain, and rain. In addition, we further examined the NSF SOCRATES campaign field catalogue for each flight to ensure that we do not miss any precipitation segments that have been identified in the field catalogue. The time stamps of the beginning and end of these segments are stored in supplemental Table S1. For most flights, we identified on average about 5 – 20 minutes of samples of precipitating regions, except RF15 which has about an hour of precipitating samples. It is worth noting that most of these segments occur at temperatures above 0°C, while this study only focuses on -40°C to 0°C.

Aerosols number concentration and size distribution are measured by the Ultra-High Sensitivity Aerosol Spectrometer (UHSAS) which has a size range of 60 – 1000 nanometers (nm). The vertical velocity measurements are derived from several instruments, including Honeywell LASEREF IV Inertial Reference Unit, radome pressure, static pressure, pitot tubes, temperature probe, and differential Global Positioning System, providing an accuracy of  $\sim\pm 0.15$ – $0.30$  m/s and precision  $\sim 0.01$  m/s (Diao et al., 2015). When examining the in-cloud and clear-sky conditions in the SOCRATES campaign, we noticed a low bias of the original vertical velocity measurements, and therefore applied a correction of +0.125 m/s for the vertical velocity values. After this correction, the peak of the frequency distributions of vertical velocity is centered at 0 m/s for both in-cloud and clear-sky conditions.

## 2.2 Two Previous Datasets for Cloud and Hydrometeor Thermodynamic Phase Classifications

For this work, two previously published datasets regarding thermodynamic phase classifications for the SOCRATES observations are used. Both datasets cover all research flights in the SOCRATES campaign with the exception of research flight 15 due to the malfunction of 2DS probe. The first dataset reports cloud phase (ice, liquid or mixed) at 1-Hz resolution, which was mainly derived from the 2DS and CDP cloud probes (Yang et al., 2021). That method used in Yang et al. (2021) was built upon the study of D’Alessandro et al. (2019) and their figure 1. The cloud phase identification was also verified by other cloud probes, such as the King probe for detecting ~~LWC~~liquid water content, and the Rosemount Icing Detector for detecting the existence of supercooled liquid ~~water droplets~~ by freezing them when they collide with the detector, and which subsequently changes its constant the vibration frequency of the detector. Two modifications are applied to the previous cloud phase identification method of D’Alessandro et al. (2019) and Yang et al. (2021). The first modification is that only when CDP measurements are categorized as liquid droplets, these samples are used in the analysis. Measurements categorized by CDP as ice particles are excluded since previous work has shown that these measurements related to counting ice are most likely artifacts (e.g., Korolev et al., 2013). The second modification is about the treatment of large particles identified as liquid droplets. The previous method restricts particles with maximum dimensions ( $D_{\max}$ )  $> 312.5$   $\mu\text{m}$  as ice particles, while those with  $D_{\max}$  between 112.5 and 312.5  $\mu\text{m}$  can be either liquid or ice depending on the standard deviation of particle sizes measured by 2DS in that second. In this work, we further restrict particles with  $D_{\max} > 212.5$   $\mu\text{m}$  to be ice particles, reducing the number of large particles being categorized as liquid droplets.

The second dataset ~~for that~~ detects individual hydrometeor’s thermodynamic phase (either ice or liquid) is also used, which was produced by the University of Washington with the Ice-Liquid Discriminator (UWILD) through a machine learning

Formatted: Not Highlight

Formatted: Subscript

Formatted: Subscript

approach (Atlas et al., 2021; Mohrmann, et al., 2021). Each particle imaged by the 2DS probe is classified particle-by-particle into ice, liquid or unclassified, as 0, 1 and NaN, respectively. In this dataset, the group also provides 1-Hz aggregated data for each research flight that include a quantification of phase-separated particle size distributions (PSDs). We use the hydrometeor count defined by the maximum diameter in the UWILD dataset to calculate  $N_{liq}$  and  $N_{ice}$  detected by the 2DS probe within each second. Then we further add  $N_{liq}$  detected by CDP to those detected by 2DS to derive the total  $N_{liq}$ . Finally, we define the ice particle number fraction, which equals  $N_{ice} / (N_{ice} + N_{liq})$  is dividing the number of ice particles by the total number of ice particles plus liquid droplets in one second.

### 3 Results

#### 3.1 A Method of Mixed-Phase Cloud to Classify Transition Phases in Classification Mixed-Phase Clouds

A classification method of to classify four the transition phases of mixed-phase clouds is developed for 1-Hz aircraft-based observations, which mainly involves two steps. In the first step, three types of cloud segments are identified for each second of observations, including liquid cloud region (LCR), ice cloud region (ICR), and mixed-phase cloud region (MCR). LCR is defined as a second of a 1-Hz in-cloud segment where only supercooled liquid droplets were observed, while ICR is defined as a segment with only ice crystals. MCR is the segment with occurrence of both ice and liquid. Here the identification of liquid and ice at 1-Hz resolution is based on the 1-Hz cloud thermodynamic phase identification method modified from D'Alessandro et al. (2019) and Yang et al. (2021) as described in Section 2.2 data published in Yang et al. (2024). In the second step, a total cloud region (TCR) that can potentially contain a combination of LCR, ICR and MCR is identified, which basically is a consecutive in-cloud segment surrounded by clear-sky conditions. For instance, if five seconds of LCR are adjacent to one second of MCR, then both the LCR and MCR belong to the same TCR. If a TCR sample is surrounded by two adjacent seconds of NaN, then this sample is deleted, because one cannot determine if the NaN points are the edge of the cloud or if they are still part of the cloud. But if a TCR sample is surrounded by two adjacent seconds of clear-sky samples, then this in-cloud sample is valid, and its measurement can last from one second to many seconds. For instance, if five seconds of LCR are adjacent to one second of MCR, then both the LCR and MCR belong to the same TCR. An illustration of the identification of TCR is shown in supplemental Figure S1. All the 1-Hz samples within the TCR are used in the analysis in the following sections. The length of each second of sample within an TCR is calculated based on the aircraft true air speed at that specific second. The length of each TCR is calculated as the sum of all in-cloud samples within that TCR. The mean true air speed of the G-V research aircraft between -40°C and 0°C during the SOCRATES campaign is ~172 m/s.

Within each TCR, the spatial ratio of LCR, MCR, and ICR relative to TCR is defined as M1, M2 and M3, respectively.

Following the calculation of these spatial ratios, four transition phases are defined as follows: (1) only LCR appears in the TCR, (2) MCR coexists with LCR, but no ICR exists, (3) ICR appears and it either resides with LCR, MCR, or both, (4) only ICR appears in the TCR. In other words, phases 1 and 4 stand for pure liquid and ice cloud segments, respectively. Phase 2

represents ~~the first appearance of those~~ ice crystals ~~as they are~~ embedded in MCR and surrounded by supercooled liquid droplets. Phase 3 represents the ~~evolution from MCR to ICR, as stage when~~ pockets of pure ice segments start to appear.

195 The four transition phases are depicted in a ~~conceptual n-idealized~~ diagram in Figure 2. The calculation of ~~M1, M2 and M3~~ spatial ratios, ~~and~~ the definition of each transition phase ~~and their number of samples~~ are summarized in Table 1.

~~Several potential evolution pathways have been documented and discussed in previous literature, which can be linked with the separation of the four transition phases described above. A “classical” type of evolution pathway follows phases (1)=>(2)=>(3)=>(4), which was observed and documented over 35 years ago (e.g., Hobbs and Rangno, 1985). This type of~~

200 ~~evolution describes the situation that a cloud is initiated as liquid phase under supercooled conditions; then it experiences ice nucleation and turns into mixed-phase; after that some section of the mixed-phase cloud glaciates and turns into ice; and in the final stage, the entire cloud is glaciated. Besides the classical progression of mixed-phase, there are two other routes of evolution of mixed-phase clouds. The second pathway is when, after nucleation of INPs and turning liquid clouds into mixed-~~

~~phase, all ice particles precipitate out of the clouds, turning the mixed-phase back into liquid. In other words, the thermodynamic phase evolution of such clouds can be described as liquid => mixed-phase => liquid, i.e., phases (1)=>(2)=>(1). The imbalance between the water vapor supply and the bulk ice mass crystal growth, required for the maintenance of mixed-phase clouds, was discussed in Rauber and Tokay (1991), Pinto (1998), and Westbrook and Illingworth~~

205 ~~(2011). There is a fair amount of modelling attempts to find an explanation of maintenance of mixed-phase clouds through the balance of INPs and dynamic forcing (e.g., Avramov et al., 2011; Fan et al., 2009, 2011; Smith et al., 2009). The third pathway~~

210 ~~of mixed-phase evolution is related to the generation of mixed-phase clouds in a pre-existing ice cloud due to dynamic forcing, which can be presented as ice=>mixed-phase, i.e., phases (4)=>(2), or (4)=>(3)=>(2). Note that the numerical order of phases 1 – 4 does not necessarily represent the evolution direction. For example, phase 4 may either be the final stage in the first classical pathway, whereas in the third pathway, phase 4 is an initial stage. The theoretical basis explaining such process was developed in several previous studies (e.g., Korolev and Mazin, 2003; Korolev and Field, 2008, Field et al., 2014; Hill et al.,~~

215 ~~2014). These studies were supported by earlier observations of mixed-phase clouds embedded in pre-existing, deep ice clouds (e.g., Hogan et al., 2002; Field et al., 2004). We~~ A potential evolution pathway from phase 1 to 4 is depicted in this idealized diagram, ~~but we caution that a mixed-phase cloud may or may not may or may not follow this/these exact pathways in the real atmosphere, as certain transition phases may be skipped, the evolution direction could be reversed, and multiple phases can appear in the same cloud in a 3-D view. Nevertheless, this method provides a statistical separation of the cloud transition~~

220 ~~phases and allows a more focused analysis of the coexistence of supercooled liquid water and ice crystals that cannot be achieved solely based on second-by-second measurements (i.e., if one only analyzes seconds with coexisting ice and liquid). Figure 3~~ a and b shows the number of 1-second samples for each transition phase as well as their probability among all transition phases within 5-degree temperature bins. The results show that phases 1 and 4 are more dominant at higher and lower temperatures, respectively, which follows the basic thermodynamic process that the transition from liquid to ice phase

occurs more frequently at lower temperatures. At temperatures between -20°C and -5°C, phase 2 is the most dominant phase and contributes to 80% to 40% of the total samples, while phase 3 contributes to 20% to 40% of the total samples. The fact

occurs more frequently at lower temperatures. At temperatures between -20°C and -5°C, phase 2 is the most dominant phase and contributes to 80% to 40% of the total samples, while phase 3 contributes to 20% to 40% of the total samples. The fact

occurs more frequently at lower temperatures. At temperatures between -20°C and -5°C, phase 2 is the most dominant phase and contributes to 80% to 40% of the total samples, while phase 3 contributes to 20% to 40% of the total samples. The fact

that the pure ice or liquid phase only contribute to 540% — 3250% of the total samples between -20°C and -5°C demonstrates that the cloud segments sampled in the SOCRATES campaign are spatially heterogeneous, consistent with the results in the previous study of D’Alessandro et al. (20210). Figure 3 c and d show the distributions of the length of TCRs in four phases. The distribution of TCR lengths is consistent with the previously observed power-law distribution of cloud horizontal sizes shown in Wood and Field (2011). Since the 1-D aircraft sampling can be at any vertical level relative to a cloud layer, we further examine the impacts of restricting the analysis to different ranges of LWC, IWC, and  $RH_4$  values (supplementary Figures S2 – S4). Previous studies such as Wang et al. (2012) and D’Alessandro et al. (2023) have shown that cloud top usually contains higher LWC than cloud base, while IWC increases from the cloud top to cloud base. D’Alessandro et al. (2019) also showed that in-cloud samples with higher liquid mass fraction have higher RH values closer to liquid saturation. By using different ranges of LWC, IWC and  $RH_4$  as proxies for vertical levels within cloud layers, we found that the number of samples of the four transition phases are relatively similar unless very high LWC or IWC are used ( $> 0.1 \text{ g m}^{-3}$ ). After defining the four transition phases, the following sections will examine both micro- and macrophysical properties of these transition phases, as well as their correlations with each other. Microphysical properties of mixed-phase clouds generally refer to hydrometeor mass concentrations, number concentrations, and size distributions. These microphysical properties can be represented by IWC, LWC, Nice, Nliq, and PSDs. On the other hand, macrophysical properties of mixed-phase clouds generally refer to the spatial extent or the spatial fraction of clouds containing supercooled liquid droplets and ice particles. The macrophysical properties can be represented by the lengths of LCR, ICR, MCR, and TCR. In addition, we define two terms – mixed spatial ratio and ice spatial ratio, to represent the spatial fraction of ice-containing clouds in phases 2 and 3, respectively. Specifically, the mixed spatial ratio represents the fraction of MCR as part of an individual, consecutive TCR in phase 2, calculated as length of MCR / length of TCR. Ice spatial ratio represents the fraction of ice-containing segments as part of an individual, consecutive TCR in phase 3, calculated as (length of ICR + length of MCR \* IWC/TWC) / length of TCR. The contribution of MCR to ice spatial ratio in phase 3 is weighted by the ice mass fraction, giving the MCR a smaller weighting function compared with ICR since MCR contains higher fractions of supercooled liquid droplets than ICR. Note that the definitions of mixed spatial ratio and ice spatial ratio differ from the spatial ratio previously used for characterization of mixed-phase clouds in Korolev et al. (2017, Fig.5-13a). In that previous method, the spatial ratio of a certain phase (liquid, mixed or ice) is calculated as the number of samples of that phase divided by the total cloud samples in a certain temperature bin. In this work, the mixed spatial ratio and ice spatial ratio are calculated for individual TCR segments, and therefore each TCR would produce one value for mixed spatial ratio and one value of ice spatial ratio. These values of mixed spatial ratio or ice spatial ratio are applied to every 1-second sample within this TCR.

### 3.25 Thermodynamic and Dynamic Effects on the Evolution of Mixed-phase Clouds

Thermodynamic and dynamic conditions of each transition phase are examined at various temperatures in Figures 4 and 5-10. Figure 4 shows the entire ~~based on~~ distributions of  $RH_{liq}$ ,  $RH_{ice}$ , vertical velocity ( $w$ ) and standard deviation of vertical velocity  $w$  ( $\sigma_w$ , calculated for every 40 seconds). ~~Previous theoretical and observational studies (Korolev and Mazin, 2003;~~

Formatted: Subscript

Formatted: Subscript

Formatted: Superscript



260 Korolev and Isaac, 2006) showed that  $RH_{liq}$  in mixed-phase clouds is close to 100%, due to evaporating droplets rapidly via the Wegner-Bergeron-Findeisen (WBF) process, bringing the system of “droplets-water vapor” to quasi-equilibrium and therefore saturating the environment. As liquid droplets glaciate into ice particles, the peak of RH frequency would also shift towards ice saturation (e.g., D’Alessandro et al., 2019). The in-cloud samples used in this study contain some sub-saturated conditions that deviate from liquid saturation in phases 1 – 3 or from ice saturation in phase 4 (as shown in Figure 4 a – d),

265 which may be attributed to a combination of reasons, such as 6%–7% uncertainties in RH values originated from water vapor and temperature measurement uncertainties, heterogeneous distributions of LCR, MCR and ICR that lead to an uneven distribution of supercooled liquid water, as well as non-equilibrated states between vapor/liquid or vapor/ice phase due to a larger volume being sampled by fast aircraft measurements (~172 m horizontal resolution for 1-Hz measurements used here). Even though all four phases show some amount of sub-saturation, phase 1 shows the least amount of ice sub-saturated

270 conditions compared with other phases. For all four phases,  $RH_i$  values above ice saturation and closer to liquid saturation have been seen, providing observational evidence that new formation of supercooled liquid water droplets and ice crystals may occur in any of the four transition phases, following either of the three evolution pathways mentioned in Section 3.1. The variability of  $\sigma_w$  values is slightly larger (0 – 2.5 m/s) in phases 2 and 3, compared with phases 1 and 4 (0 – 1.25 m/s), indicating more turbulent conditions when supercooled liquid water and ice crystals coexist in phases 2 and 3.

275 Figure 5 a – d show the average values of  $RH_{liq}$ ,  $RH_i$ , vertical velocity ( $w$ ) and  $\sigma_w$  at various temperatures, respectively. The number of samples used for Figure 5 is shown in supplemental Figure S5. In addition, a similar analysis in relation to ice spatial ratio is shown in Figure 11. For the distribution of  $RH_i$  and  $RH_{liq}$ , phase 2 shows the highest RH values, followed by phases 1 and 3. Phase 4 has the lowest  $RH_i$  and  $RH_{liq}$  values. Comparing  $RH_i$  values in regions with and without ice, phase 2 shows higher  $RH_i$  for regions with ice, while phase 3 shows higher  $RH_i$  in regions without ice. This feature can be explained by the fact that higher  $RH_i$  is required in order to initiate ice nucleation in phase 2, while ice crystals that continue to grow in phase 3 will further reduce  $RH_i$  magnitude by vapor deposition. Based on the analysis in Section 3.3 and Figure 87, the average ice mass fraction (i.e., IWC/TWC) is also lower in phase 2 than phase 3, which suggests that ice crystals in phase 2 would be less effective for relaxing ice supersaturation than those in phase 3.

280 For distributions of  $w$  in Figure 5 c, phase 1 has slightly higher  $w$  than other phases. Phases 2 – 4 show slightly negative average  $w$  values, suggesting weak downdrafts as the predominant average condition in mixed-phase clouds these phases. For the  $\sigma_w$  distribution (Figure 5 d), regions with ice in phase 2 have the highest fluctuations of vertical velocity, indicating that stronger in-cloud turbulence induces high  $RH_i$  (as shown in Figure 5 a), which further initiates ice nucleation in phase 2. This result suggests that in-cloud turbulence may be a more prominent mechanism to initiate transition from liquid to ice phase, compared with large-scale uplift (which would be reflected in mean vertical velocity in Figure 5 c if that was the case). Such result is consistent with the finding of Bühl et al. (2019) which showed a positive correlation between IWC mass flux and vertical velocity fluctuation, but this study further illustrates that in-cloud turbulence is particularly important for the early transition phase 2 when ice crystals first start to appear inside MCR, surrounded by supercooled liquid water.

285

290

Formatted: Subscript

Formatted: Subscript

295 ~~For~~ The relationship between RH and ice spatial ratio ~~the spatial expansion of ice-containing regions is examined in (Figure 5 e and f, 11 a and b).~~ Phase 2 shows nearly constant  $RH_{liq}$  close to liquid saturation when mixed spatial ratio increases (i.e.,  $RH_{liq}$  is within 5% of liquid saturation, which may be caused by combined uncertainties from water vapor and temperature measurements), except when ice spatial ratio exceeds 0.9. Differing from phase 2, phase 3 shows decreasing  $RH_{liq}$  with increasing ice spatial ratio, ranging from 98% to 85%  $RH_{liq}$ . These results indicate that before the appearance of ICR, ice crystals embedded in MCRs do not relax liquid saturation to ice saturation since liquid droplets can still provide additional water vapor by evaporation. (e.g., the WBF Bergeron-process). But when ICR starts to appear, RH relaxes to around ice saturation once ice spatial ratio exceeds 0.5. These results are consistent with the previous finding by D'Alessandro et al. (2019) that  $RH_{liq}$  initially is close to liquid saturation with lower ice mass fraction but deviates from liquid saturation as ice mass fraction increases.

300 ~~For~~ The mean values of  $w$  do not vary significantly with mixed spatial ratio or ice spatial ratio (Figure 5 g, 11 e), higher  $w$  is seen at lower ice spatial ratio), but the PDFs of vertical velocity in supplemental Figure S6 b show higher frequencies of updrafts for phases 2 and 3 compared with phases 1 and 4, meaning that the segments containing more both supercooled liquid droplets and ice particles are subject to relatively more updrafts, while compared with the segments containing more only liquid droplets or only ice crystals are subject to more downdrafts. This finding is consistent with Shupe et al. (2008) which pointed out the importance of updrafts for sustaining mixed-phase clouds. Differing from the previous studies, our method can further specify that the highest updrafts and vertical velocity fluctuations are found in transition phase 3 when pure ice segments start to appear (~4.5 m/s in Figure S6 b and ~2.3 m/s in Figure S6 c). Differing from the previous studies, our method can further specify that the highest updrafts are found in the later transition phase when pure ice segments start to appear, consistent with the fact that  $RH_{liq}$  deviates more from liquid saturation in phase 3 (Figure 5 f, 11 b), and therefore higher updrafts would be required to maintain supercooled liquid droplets. Analysis of  $\sigma_w$  distribution (Figure 5 h, 11 d) consistently shows that ice-containing regions in phase 2 have the highest vertical velocity fluctuations compared with other phases, especially for at higher ice mixed spatial ratios, suggesting that even more turbulent condition is needed when supercooled liquid water is surrounded by a large spatial extent of ice-containing regions. Overall, the fact that mean  $w$  values are not significantly different between segments with or without ice in phases 2 and 3 (Figure 5 c) but are more different between phases 2 & 3 versus phases 1 & 4 (Figure S6 b) suggests that higher mean  $w$  is more important for sustaining the supercooled liquid water in coexistence with ice particles than for initiating ice nucleation. But for other phases, vertical velocity fluctuations are higher for low ice spatial ratios. These results indicate that both the initiation of ice nucleation and the sustainability of supercooled liquid water are supported by in-cloud turbulence, while updrafts large-scale ascent plays an important role in the latter but not the former.

Formatted: Subscript

### 3.2 Occurrence Frequencies of Cloud Phases Compared Among Various Phase Identification Methods

325 The distributions of three cloud thermodynamic phases (ice, liquid and mixed) are compared between three types of phase identifications, including (i) the 1-Hz cloud phase distribution defined by Yang et al. (2021) using the ice mass fraction (i.e., IWC/TWC) derived for 1-second observations, i.e., liquid, mixed and ice phases defined as ice mass fraction  $< 0.1$ ,  $0.1 - 0.9$  and  $> 0.9$ , respectively; (ii) cloud phase distribution defined by the majority of the hydrometeors by particle count using the UWILD data, i.e., liquid (ice) phase defined as a second of data with more than 90% (less than 10%) of hydrometeor particle count being liquid droplets, and mixed phase defined as a second of data with 10%–90% of particle count being liquid droplets; (iii) cloud phases defined by the ice spatial ratio within each TCR using the method developed in this work. That is, for each TCR, ice spatial ratio is calculated as length of (ICR+MCR) / length of TCR. Liquid, mixed, and ice phases are defined as where ice spatial ratio of an entire TCR is  $< 0.1$ ,  $0.1 - 0.9$  and  $> 0.9$ , respectively. To summarize, each of these three types of method relies on a certain type of fraction of ice crystals relative to the total hydrometeors, either in terms of 1-Hz mass fraction, 1-Hz particle number fraction, or in terms of the spatial fraction relative to the entire cloud segment.

335 Figure 4 shows the occurrence frequencies of cloud thermodynamic phases in relation to temperature compared among three identification methods. The results show that the ice spatial ratio (Figure 4 a) and ice mass fraction (Figure 4 c) methods have similar distributions of three thermodynamic phases. The ice spatial ratio method has slightly higher mixed-phase frequency than the ice mass fraction method. For the ice particle number fraction method (Figure 4 b), the mixed-phase frequency is the highest among all three methods, at  $0.1 - 0.2$ . At temperatures above  $-20^{\circ}\text{C}$ , ice crystals often have larger size dimension but smaller number concentration than supercooled liquid droplets, meaning that when ice number fraction is less than 0.1 (liquid phase in Figure 4 b), ice mass fraction may exceed 0.1 and becomes mixed phase in Figure 4 c. For the lowest temperature bin close to  $-40^{\circ}\text{C}$ , the particle-by-particle identification may have difficulties discerning single hydrometeors as frozen droplets, supercooled liquid droplets or small ice crystals, which leads to the large increase in mixed phase frequency in that bin. Overall, all three methods show a significant transition from liquid to ice phase at a similar temperature around  $-17.5^{\circ}\text{C}$ . This indicates that the major transition from liquid to ice are reflected in both cloud microphysical (i.e., mass partition and number partition) and macrophysical properties (spatial extent partition).

### 3.3 Relationship between Microphysical and Macrophysical Properties of Mixed-phase Clouds

340 The cloud particle size distribution (PSD) for four transition phases is shown in Figure 6, separately plotted for the 2DS and CDP probes. Measurements from both probes have been identified in any of the four transition phases, since either probe can possibly measure ice or liquid. Phase 1, 2 and 3 both have similar the highest concentrations of small liquid droplets between  $2 - 10 \mu\text{m}$ . Phase 2 has the highest concentrations of hydrometeors at  $10 - 60 \mu\text{m}$ , while phase 3 has the highest concentrations at  $60 - 3000 \mu\text{m}$ . Phase 4 also has relatively high concentrations of ice crystals at  $200 - 3000 \mu\text{m}$ , but they are lower than the values from phase 3 by a factor of 5 – 10. The decreasing ice crystal concentrations per size bin from phase 3 to phase 4 may be caused by stronger aggregation, sublimation, and/or sedimentation of ice crystals in phase 4, or as well as

by stronger glaciation and/or secondary ice production in phase 3. The significant decrease (1 to 4 orders of magnitude) of hydrometeor concentrations per size bin at 20 – 1060  $\mu\text{m}$  in phase 4 compared with the other three phases suggests that most supercooled liquid water may have evaporated and transitioned into ice phase through Bergeron-WBF process or riming, instead of the freezing of individual droplets, while the small ice crystals may have sublimated. It is possible that some of the  
360 phase 4 samples may represent the trails of generating cells, where the growth is aloft, and sublimation is at the lower part of the cloud layer. In addition, smaller supercooled liquid droplets require lower temperatures to freeze into ice crystals. This feature is also shown in Figure 6 a–d, as small ice crystals at 20 – 2060  $\mu\text{m}$  size range show increasing concentrations with decreasing temperatures. Phase 4 shows a trend of decreasing frequency of large ice particles (e.g.,  $D_{\text{max}} > 2000$   $\mu\text{m}$ ) with decreasing temperature. This could be due to an increasing probability of droplet freezing with decreasing temperature given  
365 the same dimension that reduces the available amount of large supercooled liquid droplets for glaciation or riming at lower temperatures. On the other hand, phase 3, which still has supercooled liquid water coexisting with ice particles, does not show such trend, probably because ice crystal growth may occur via various processes in phase 3, such as WBF process, glaciation, vapor depositional growth under ice supersaturation, and/or riming. An additional cloud probe—the Fast 2-Dimensional-Cloud (Fast-2DC) probe is also examined in Figures 5 and 6. Even though the 2DC probe had more problematic measurements compared with 2DS probe due to cloud imaging issues during SOCRATES, the two probes (2DS and 2DC) still show similar PSD results for three transition phases containing ice crystals (i.e., phases 2, 3 and 4), indicating that the differences seen among transition phases are less likely caused by instrument uncertainties.  
370 One unique contribution of this work is to quantify how cloud microphysical and macrophysical properties are correlated with each other. The relationship between cloud macrophysical properties (represented by mixed or ice spatial ratio) and several microphysical properties are further examined, including ice particle number fraction (Figure 7), as well as LWC, IWC and ice mass fraction (Figure 8). L-A linear regressions of the mixed spatial ratio and ice spatial ratio against each microphysical property are shown for transition phases 2 and 3, respectively. The analysis is separated by LCR, MCR and ICR. Slope The slope value (b) of the linear regression is provided in the text legend. Since transition phase 2 does not contain ICR, no data points are shown in those sub-panels in Figures 7, 8 and 10–9.  
375 All regions (i.e., LCR, MCR and ICR) in Figure 7 show positive correlations between ice particle number fraction and mixed or ice spatial ratio in phases 2 and 3. This means that while ice crystals gradually dominate the total particle population (supercooled liquid droplets plus ice particles) in a particular secondTCR, the segments containing ice particles (i.e., MCR+ICR) also start to dominate the spatial extent of the entire cloud segment (TCR) from a macroscopic perspective. Comparing phase 2 and 3, phase 2 (without ICRs) shows smaller positive correlation (b values of 0.0090-24 and 0.0130-35)  
380 compared with phase 3 (b values of 0.561, 0.026, and 0.469-0.67, 0.47, and 0.52). This is because when ice particles are surrounded by supercooled liquid water droplets, the latter has much much higher number concentration than ice crystals and therefore ice particle number fractions are relatively low, ranging from 0 to 0.2 on average in phase 2. On the other hand, in phase 3, ice crystals start to become the dominant particles by number concentration when ICR appears, and supercooled liquid water droplets becomes less dominant. Similar slope values in Figure 7 b, d and f indicate that the rates of change of ice particle

Formatted: Subscript

390 number fraction in LCR, ~~MCR~~ and ICR are similar. That is, as the entire segment TCR becomes more ice dominant, individual ~~small LCR and ICR~~ segments embedded inside also experience similar rates of transition from liquid to ice based on number concentrations, except that the ICR has higher ice particle number fraction on average (i.e., higher intercept values), ~~followed by MCR, then LCR.~~

395 Previously, Wang et al. (2020) used airborne remote sensing measurements from ~~the~~ SOCRATES campaign to identify generating cells of ice crystals. Their study showed that inside the generating cells, larger ice particles and higher ice number concentrations were seen, associated with the updrafts inside the cells. These reported generating cells are also analyzed in Figure 7, which shows their average values in each ice spatial ratio bin. The generating cells associated with ~~smaller ice spatial ratio~~ LCR and MCR contain lower ice particle number fractions (Figure 7 a – d). But when the generating cells are associated with ~~ice-dominated segments (i.e., ICR)~~ higher ice spatial ratio ( $\geq 0.5$ ), significantly higher ice particle number fractions ~~(around 0.6 close to 1)~~ are seen for most ice spatial ratio bins (Figure 7 f). This result suggests that not all regions within the generating cells experience significant phase transition from liquid to ice, unless the ice-containing regions become dominated ~~by ice in terms of spatial extent.~~

400 Figure 8 shows the correlations of LWC and IWC with respect to ~~mixed spatial ratio or~~ ice spatial ratio. A clear negative slope is seen in Figure 8 a–d, indicating that as the ~~mixed spatial ratio or~~ ice spatial ratio increases, the LWC decreases. On the contrary, a positive trend is seen in Figure 8 e, f and h, indicating increasing IWC with increasing ~~mixed or~~ ice spatial ratio. 405 These results are consistent with the analysis of ice particle number fraction, ~~which showing~~ that the increasing dominance of ice crystals in both mass and number concentrations is correlated with the increasing spatial ratio of ice-containing regions ~~in each TCR.~~ Slope values in Figure 8 illustrate that in phase 2 and 3, LWC decreases more significantly in LCR ( $b = -0.46060$ ) than MCR ( $b = -0.05544$ ). Compared with phase 2, phase 3 shows ~~an~~ even stronger decrease of LWC in LCR and MCR with  $b = -1.6945$  and  $-0.69270$ , respectively. For the changes of IWC, the slope values are similar between MCR and ICR in phase 3 ( $b = 1.3584$  and  $1.2615$ , respectively), and are slightly lower for MCR in phase 2 ( $b = 0.96944$ ). These results indicate that IWC has ~~similar a similar~~ rate of increase between ice crystals embedded among supercooled liquid droplets (i.e., MCR) and ice crystals in pure ice segments (i.e., ICR) ~~in phases 2 and 3.~~ However, the ~~rate of~~ decrease of LWC ~~with the spatial expansion of ice-containing regions~~ becomes more significant by a factor of 3 once pure ice segments appear in phase 3 compared with 415 phase 2.

Figure 8 ~~ic~~ i and j show the positive correlations ~~between-of~~ ice mass fraction ~~and-with respect to mixed spatial ratio or~~ ice spatial ratio. Ice mass fraction increases more rapidly with increasing spatial ~~ratio-fraction of ice-containing regions~~ in phase 3 than phase 2, with slope values of  $1.013088$  and  $0.23849$ , respectively. This result indicates that when ice crystals first appear in MCR, the mass partitioning is still dominated by liquid phase even if ice crystals appear in a high spatial fraction of the cloud segment ~~as part of MCR.~~ As ice crystals grow into pure ice segments (i.e., ICR), liquid phase starts to rapidly transition into ice phase, suggesting that the ~~formation and growth of ice particles become more significant when formation-of~~ pure ice segments ~~- appear is a key step for Bergeron process to become highly effective.~~ This result also indicates that even 420

though ice and supercooled liquid water coexist throughout the lifetime of mixed-phase clouds, the partition between them has different rates of phase change during different transition phases.

To assess the impacts of the sub-saturated conditions within TCR on the main findings of this work, we examine the impacts of excluding the lower  $RH_i$  samples from the analysis of cloud micro- and macrophysical properties. Supplemental Figures S7 and S8 show the results of excluding  $RH_i < 80\%$  based on the analysis similar to Figures 7 and 8, respectively. The relationships of ice particle number fraction, IWC, LWC and ice mass fractions with respect to mixed spatial ratio and ice spatial ratio show similar results when lower  $RH_i$  are excluded, demonstrating the robustness of these main conclusions.

Formatted: Subscript

Formatted: Subscript

Formatted: Subscript

### 3.4 Comparisons of Three Methods to Define Cloud Thermodynamic Phases

The distributions of three cloud thermodynamic phases (ice, liquid, and mixed) are compared between three types of phase identifications, including (i) the 1-Hz cloud phase distribution defined by the ice mass fraction (i.e.,  $IWC/TWC$ ) derived for 1-second observations, i.e., liquid, mixed and ice phases defined as ice mass fraction  $< 0.1$ ,  $0.1 - 0.9$  and  $> 0.9$ , respectively; This method of using ice mass fraction to define mixed-phase clouds has been used in the cloud physics community for approximately thirty years (e.g., Korolev et al., 1998; Korolev et al., 2017, their equation 5-1 and references therein); (ii) cloud phase distribution defined by the majority of the hydrometeors by particle number concentrations using the combined CDP and 2DS data, i.e., liquid (ice) phase defined as a second of data with more than 90% (less than 10%) of hydrometeor particle number concentrations being liquid droplets, and mixed phase defined as a second of data with 10% – 90% of particle number concentrations being liquid droplets; (iii) cloud phases defined by the ice spatial ratio within each TCR using the method developed in this work. Liquid, mixed, and ice phases are defined as where the ice spatial ratio of an entire TCR is  $< 0.1$ ,  $0.1 - 0.9$  and  $> 0.9$ , respectively. To summarize, each of these three types of methods relies on a certain type of fraction of ice crystals relative to the total hydrometeors, either in terms of 1-Hz mass fraction, 1-Hz particle number fraction, or in terms of the spatial fraction relative to the entire cloud segment. This concept of using various ice fractions to define cloud thermodynamic phases has been summarized in the previous review article by Korolev et al. (2017).

Figure 9 shows the occurrence frequencies of cloud thermodynamic phases in relation to temperature compared among three identification methods. The results show that all three methods have similar distributions of three thermodynamic phases at temperatures above  $-30^\circ\text{C}$ . For the lowest temperature bins close to  $-40^\circ\text{C}$ , the particle-by-particle identification may have difficulties discerning single hydrometeors as frozen droplets, supercooled liquid droplets or small ice crystals, which leads to the large increase in mixed phase frequency in that bin. For temperatures between  $-20^\circ\text{C}$  and  $0^\circ\text{C}$ , the ice spatial ratio method has slightly higher mixed phase frequency ( $0.1 - 0.2$ ) than the ice particle number fraction method ( $\sim 0.1$ ). The ice mass fraction method has the lowest mixed phase frequency among all three methods, at  $0.03 - 0.07$ . Overall, all three methods show a significant transition from liquid to ice phase at a similar temperature around  $-17.5^\circ\text{C}$ . This indicates that the major transition from liquid to ice is reflected in both cloud microphysical (i.e., mass partition and number partition) and macrophysical properties (spatial extent partition). The rapid increase of occurrence of ice clouds in the temperature range of  $-15^\circ\text{C}$  to  $-20^\circ\text{C}$  was also observed by previous studies (e.g., Wallace and Hobbs, 1977; Moss and Johnson, 1994). The analysis of Figure 9 is

also conducted for only  $RH_i > 80\%$  in supplementary Figure S9 and the results show consistent results of the cloud phase frequency distributions regardless of the exclusion of low  $RH_i$  values.

Formatted: Subscript

Formatted: Subscript

### 3.5.4 Aerosol Indirect Effects on the Evolution of Mixed-phase Clouds

The relationship between aerosol number concentration and mixed spatial ratio or ice spatial ratio is examined in Figure 109.

460 Due to the possible complication of in-cloud measurements of aerosol number concentrations, we applied a moving average to calculate logarithmic scales of aerosol concentrations at every 50 seconds in Figure 10. A coarser spatial averaging using the 100-second moving average is also shown in supplementary Figure S10.

465 Number concentrations of larger aerosols (diameters  $> 500$  nm, namely  $N_{>500}$ ) and smaller aerosols (diameters  $> 100$  nm, namely  $N_{>100}$ ) are analyzed in Figure 10 a – h and i – p, respectively. The slope values of the linear regressions show strong positive correlations between  $N_{>500}$  and ice spatial ratio in phase 2 (Figure 10 g,  $b = 1.198$ ), when ice crystals just start to appear and are surrounded by supercooled liquid droplets. Such positive correlation becomes weaker in phase 3 (Figure 10 h,  $b = 0.721$ ), when ICR starts to appear. The stronger positive correlation with  $N_{>500}$  in phase 2 is likely due to primary ice nucleation (such as heterogeneous nucleation) playing a major role in phase 2 when ice crystals first start to appear. On the other hand, secondary ice production may occur more frequently in phase 3, and secondary ice production via rime-splintering is less effective when concentrations of cloud condensation nuclei are higher. For the correlations with  $N_{>100}$ , a positive trend is still seen with respect to ice spatial ratio in MCR and ICR, indicating possible heterogeneous nucleation pathways of ice formation via condensation freezing and immersion freezing assisted by smaller aerosols. Negative correlations between  $N_{>100}$  and ice spatial ratio in LCR suggest that without ice nucleating particles to facilitate ice formation (hence the pure liquid segment LCR), higher aerosol number concentration may impede the growth of ice segments. Overall, the weaker positive correlations with  $N_{>100}$  in MCR and LCR compared with  $N_{>500}$  indicates that larger aerosols play a more dominant role for initiating ice nucleation than smaller aerosols. Stronger positive correlations between IWC and  $N_{>500}$  compared with  $N_{>100}$  are also shown in the previous work by Yang et al. (2021), although that study did not differentiate the transition phase of clouds nor examine aerosol indirect effects in relation to cloud macrophysical properties, i.e., the spatial expansion of ice-containing cloud segments.

Formatted: Subscript

Formatted: Subscript

### 480 3.5 Thermodynamic and Dynamic Effects on the Evolution of Mixed-phase Clouds

485 Thermodynamic and dynamic conditions of each transition phase are examined at various temperatures in Figure 10, based on distributions of  $RH_{liq}$ ,  $RH_i$ , vertical velocity ( $w$ ) and standard deviation of  $w$  ( $\sigma_w$ , calculated for every 40 seconds). In addition, a similar analysis in relation to ice spatial ratio is shown in Figure 11. In the distribution of  $RH_i$  and  $RH_{liq}$ , phase 2 shows the highest  $RH$  values, followed by phases 1 and 3. Phase 4 has the lowest  $RH_i$  and  $RH_{liq}$  values. Comparing  $RH_i$  values in regions with and without ice, phase 2 shows higher  $RH_i$  for regions with ice, while phase 3 shows higher  $RH_i$  in regions without ice. This feature can be explained by the fact that higher  $RH_i$  is required in order to initiate ice nucleation in phase 2, while ice crystals that continue to grow in phase 3 will further reduce  $RH_i$  magnitude by vapor deposition. Based on Figure 7, IWC is

also lower in phase 2 than phase 3, which suggests that ice crystals in phase 2 would be less effective for relaxing ice supersaturation than those in phase 3.

490 For distributions of  $w$ , phase 1 has slightly higher  $w$  than other phases. Phase 2—4 show slightly negative  $w$  values, suggesting weak downdrafts as the predominant condition in mixed phase clouds. For the  $\sigma_w$  distribution, regions with ice in phase 2 have the highest fluctuations of vertical velocity, indicating that stronger in-cloud turbulence induces high RH<sub>liq</sub> (as shown in a), which further initiates ice nucleation in phase 2. This result suggests that in-cloud turbulence may be a more prominent mechanism to initiate transition from liquid to ice phase, compared with large-scale uplift (which would be reflected in mean vertical velocity if that was the case). Such result is consistent with the finding of Bühl et al. (2019) which showed a positive correlation between IWC mass flux and vertical velocity fluctuation, but this study further illustrates that in-cloud turbulence is particularly important for the early transition phase when ice crystals first start to appear.

495 For the relationship between RH and ice spatial ratio (Figure 11 a and b), phase 2 shows nearly constant RH<sub>liq</sub> close to liquid saturation (within 5% of liquid saturation, which may be caused by combined uncertainties from water vapor and temperature measurements), except when ice spatial ratio exceeds 0.9. Differing from phase 2, phase 3 shows decreasing RH<sub>liq</sub> with increasing ice spatial ratio, ranging from 98% to 83% RH<sub>liq</sub>. These results indicate that before the appearance of ICR, ice crystals embedded in MCRs do not relax liquid saturation to ice saturation since liquid droplets can still provide additional water vapor by evaporation (e.g., the Bergeron process). But when ICR starts to appear, RH relaxes to around ice saturation once ice spatial ratio exceeds 0.5. These results are consistent with the previous finding by D'Alessandro et al. (2021) that RH<sub>liq</sub> initially is close to liquid saturation with lower ice mass fraction but deviates from liquid saturation as ice mass fraction increases.

500 For mean values of  $w$  (Figure 11 c), higher  $w$  is seen at lower ice spatial ratio, meaning that the segments containing more supercooled liquid droplets are subject to more updrafts, while the segments containing more ice crystals are subject to more downdrafts. This finding is consistent with Shupe et al. (2008) which pointed out the importance of updrafts for sustaining mixed-phase clouds. Differing from the previous studies, our method can further specify that the highest updrafts are found in the later transition phase when pure ice segments start to appear, consistent with the fact that RH<sub>liq</sub> deviates more from liquid saturation in phase 3 (Figure 11 b), and therefore higher updrafts would be required to maintain supercooled liquid droplets. Analysis of  $\sigma_w$  distribution (Figure 11 d) consistently shows that ice-containing regions in phase 2 have the highest vertical velocity fluctuations, especially for higher ice spatial ratios. But for other phases, vertical velocity fluctuations are higher for 515 low ice spatial ratios. These results indicate that both the initiation of ice nucleation and the sustainability of supercooled liquid water are supported by in-cloud turbulence, while updrafts play an important role in the latter but not the former.

#### 4 Discussion and Conclusions

Mixed-phase clouds are ubiquitous in the atmosphere and in order to fully capture their extent of impacts on Earth's climate, more studies need to be conducted in order to investigate their formation, evolution, and aerosol effects on their microphysical



520 and macrophysical characteristics. Therefore, in this study, a novel method that categorizes mixed-phase clouds ~~evolution~~ into four transition phases was presented. This method allows an investigation on the evolution of cloud macrophysical and microphysical properties, as well as the related aerosol indirect effects, as ~~the phase change occurs among vapor, liquid, and solid phase of water molecules~~ supercooled liquid water transitions to ice crystals.

The relationships between microphysical and macrophysical properties are examined, which addresses the question of whether the dominance of ice crystals in hydrometeor mass or number concentration also leads to ~~the~~ dominance of ice-containing regions in a consecutive in-cloud segment. ~~Two~~ A spatial extent parameters – ~~mixed spatial ratio and~~ ice spatial ratio – ~~are~~ is used to identify the ~~evolution from~~ spatial transition between supercooled liquid water-dominant ~~and~~ to ice-dominant mixed phase clouds. Positive correlations of ice particle number ~~concentration-fraction~~ and IWC in relation to mixed spatial ratio and ice spatial ratio are seen in both transition phases 2 and 3, respectively. Comparing phases 2 and 3, the latter phase shows higher rates of changes in all three microphysical properties with increasing ice spatial ratio, including faster increase of ice number fraction, faster increase of IWC, and faster decrease of LWC. These results indicate that when ice crystals become more dominant and ~~ICR-pure ice segments~~ starts to appear, both the mass and number partitions between liquid phase and ice phase experience a higher rate of transition.

The correlations between various ~~cloud macro- and microphysical cloud~~ properties are further demonstrated by using three methods to define ice, liquid, and mixed phases. Following the generic definition of mixed-phase clouds described in Korolev et al. (1998) and Korolev et al. (2017),  $\mu_{ice} = \alpha_{ice} / (\alpha_{ice} + \alpha_{liq})$ , where  $\mu_{ice}$  is ice phase fraction, and  $\alpha_{ice}$  and  $\alpha_{liq}$  are specific cloud microphysical properties. We examined  $\alpha_{ice}$  being ice mass fraction or ice particle number fraction at 1-Hz resolution, but also ~~extended~~ the definition to include  $\alpha_{ice}$  being ice spatial ratio in a consecutive cloud segment, which is a macrophysical property that has not been investigated before. All three methods follow the same thresholds of  $< 0.1$ ,  $0.1 - 0.9$ , and  $> 0.9$  to separate  $\mu_{ice}$  into liquid, mixed and ice phases, respectively. As a result, all three methods identify a significant transition from liquid to ice around a similar temperature at  $-17.5^{\circ}\text{C}$ . A minor difference among three methods is that mixed-phase cloud frequency between  $-20.5^{\circ}\text{C}$  to  $0^{\circ}\text{C}$  is slightly higher when defined by ice number fraction and ice spatial ratio ( $0.1 - 0.2$ ) compared with that defined by ice mass fraction ( $0.05$ ). Such comparison on various phase definition methods indicates that a spatial extent-based cloud phase identification method, such as using number of pixels in remote sensing data by Yip et al. (2021) and Desai et al. (2023), can produce similar statistical distributions of liquid and ice phases compared with other methods based on ice mass fraction, e.g., Yang et al. (2021) ~~and~~ D’Alessandro et al. (2019) and Yang et al. (2021), while the spatial extent-based method produces a slightly higher mixed-phase cloud frequency. Future analysis of cloud phase distributions based on different types of observation techniques and model simulations is recommended to consider this comparison result, especially when evaluating model output against observations using different definitions of mixed-phase clouds.

550 Differing from previous studies on the coexistence of ice crystals and supercooled liquid water, the method presented in this work allows one to separately examine the cases when ice crystals ~~first start to appear~~ are surrounded by supercooled liquid water in MCR (phase 2) and compare them with cases when ice crystals become more dominant in ICR (phase 3). Because of this, aerosol indirect effects ~~on the earlier and later transitions from supercooled liquid water to ice on various stages of clouds~~

555 can also be examined separately. Number concentrations of aerosols larger than 500 nm show stronger positive correlations with mixed spatial ratio and ice spatial ratio compared with aerosols larger than 100 nm. This indicates that the larger aerosols more are more likely to act as ice nucleating particles (INPs) to initiate primary ice nucleation. Transition phase 3 shows a slightly weaker positive correlation of ice spatial ratio with aerosol number concentrations (i.e.,  $N_{>500}$  and  $N_{>100}$ )s compared with phase 2, indicating that the aerosol indirect effects are more prominent when ice crystals first start to appear amongst supercooled liquid water in MCR. Such weaker aerosol indirect effects in phase 3 are possibly due to a competition between the positive correlation of primary ice nucleation with aerosol number concentrations and the negative correlation of secondary ice production with aerosol number concentrations. When pure ice segments (ICR) start to appear, it is possible that secondary ice production plays a more important role and therefore the net aerosol indirect effects become weaker.

Thermodynamic and dynamic conditions are examined for each transition phase, especially for two key stages of mixed-phase clouds – the initiation of ice nucleation in MCR and the coexistence of liquid and ice after pure ice segments are being formed.

565 The results show that regions with ice crystals in phase 2 are associated with the highest  $RH_i$  values as well as the highest fluctuation of vertical velocity. This result indicates that in-cloud turbulence is likely the main mechanism to produce higher  $RH_i$  in order to initiate ice nucleation. Averages of vertical velocity do not show significantly higher values for phase 2, indicating the large-scale ascent plays a less important role for initiating the transition from liquid to ice compared with in-cloud turbulence in the SOCRATES campaign. As for the dynamical conditions supporting the coexistence of liquid and ice,

570 previously, several dynamic mechanisms were proposed in the study of Korolev and Field (2008), highlighting the critical thresholds of vertical motion for sustaining supercooled liquid water. Our analysis shows that both ascent and in-cloud turbulence are more frequently observed when liquid phase becomes more dominant in terms of spatial extent (i.e., low ice spatial ratio). The highest updrafts were observed in transition phase 3 in segments containing both ice and liquid (i.e., phases 2 and 3 versus phases 1 and 4 shown in supplementary Figure S6 bMCR), indicating that higher updrafts are needed to sustain supercooled liquid water when they are surrounded by ice crystals. This observation-based method can be used to assess the contribution from different dynamic mechanisms for maintaining different evolution stages of mixed-phase clouds in various field campaigns.

580 The definition of LCR, MCR and ICR is also related to the two types of mixed-phase clouds – genuinely versus conditionally mixed, separated by the level of mixing between supercooled liquid water and ice crystals (e.g., Korolev et al., 2017, their Fig. 5-1; Korolev and Milbrandt, 2022, their Fig. 1). The scenario of “LCR+ICR” identified as one sub-category of phase 3 would be considered a conditionally mixed-phase cloud, which may form a sequence of spatially adjacent cloud segments ...-ice-liquid-ice-liquid-.... Such clouds may be thermodynamically stable, and their lifetime would be determined by processes other than the interaction between ice and liquid (e.g., WBF and riming). This special scenario when only “LCR+ICR” exist in the TCR without the existence of MCR has 840 seconds of samples, which is a small fraction of the total 11988 seconds of transition phase 3 samples. This result suggests that most of the clouds with coexisting supercooled liquid water and ice particles at least contain some partial segments as genuinely mixed phase, i.e., MCR.

Formatted: Subscript

Formatted: Not Highlight

Formatted: Not Highlight

Formatted: Not Highlight

Formatted: Not Highlight

Formatted: Not Highlight

Parameterizations of mixed-phase clouds in climate models often rely on a tunable parameter that can modify the mixing volume between ice and liquid (e.g., Tan and Storelvmo, 2016; Zhang et al., 2019). In other words, if ice crystals are mixed uniformly amongst supercooled liquid water within a model grid box, the Bergeron-WBF process would become more effective and the transition from liquid to ice would be faster. This study illustrates that the effectiveness of Bergeron process is rates of phase change are strongly affected by the existence of pure ice segments, not only by the mixed spatial ratio or ice spatial ratio which reflects how extensive the spatial coverage of ice crystals, but spatial coverage is (Figure 87). Future model parameterization development is recommended to consider the varying effectiveness of Bergeron processes rates of phase change due to the spatial and temporal variabilities of how liquid and ice spatially overlap with each other throughout a cloud's lifetime.

Overall, the method proposed in this work provides a unique perspective to assess the various evolution stages of mixed phase clouds, especially the transition from liquid to ice phase. Such transition can be reflected in particle number fraction, mass fraction, and spatial ratio. We note that this is an idealized method with its own caveats. For example, the evolution of mixed-phase clouds may not always follow this a simple direction from phase 1 to 4. In addition, the aircraft observations used here only captures the 1-D structure of a cloud segment, while cloud layers above and below the aircraft flight track may show a different ice spatial ratio on a 2-D or 3-D view. Nevertheless, this method helps to provide a statistical categorization of different evolution-transition phases of mixed-phase clouds solely based on Eulerian-view sampling of aircraft data, which enables more detailed examination on cloud evolution from a statistical, quasi-Lagrangian view that was not available previously. Future investigation that compares 1-D aircraft sampling with 2-D remote sensing observations and 3-D model simulations is recommended to further examine the quasi-Lagrangian evolution of mixed-phase clouds. Future investigation that compares 2-D remote sensing observations with collocated 1-D aircraft sampling is recommended to further assess this method against other types of measurement techniques.

#### Data availability

Observations from the NSF SOCRATES campaign are accessible at <https://data.eol.ucar.edu/>.

#### Author contributions

F. Maciel, and M. Diao, and C.A. Yang contributed to the development of the ideas, conducted quality control to aircraft-based observations, and conducted data analysis, and F. Maciel and M. Diao wrote the manuscript. F. Maciel contributed to the subsequent data analysis.

615 **Competing interests**

The authors declare that they have no conflict of interest.

**Acknowledgments**

F. Maciel, C.A. Yang and M. Diao acknowledge funding from NSF OPP #1744965. M. Diao acknowledges the funding support from U.S. Department of Energy (DOE) Atmospheric System Research (ASR) grant DE-SC0021211 and RDPP grant DE-SC0023155. C.A. Yang and M. Diao acknowledge funding from SJSU Division of Research and Innovation award number 22-LUG-08-006. F. Maciel and C.A. Yang also acknowledges support from the San Jose State University Walker Fellowship.

**References**

- Atlas, R., Mohrmann, J., Finlon, J., Lu, J., Hsiao, I., Wood, R., and Diao, M.: The University of Washington Ice-Liquid Discriminator (UWILD) improves single-particle phase classifications of hydrometeors within Southern Ocean clouds using machine learning, *Atmos. Meas. Tech.*, 14, 7079–7101, <https://doi.org/10.5194/amt-14-7079-2021>, 2021.
- Ayramov, A., Ackerman, A. S., Fridlind, A. M., Van Diedenhoven, B., Botta, G., Aydin, K., Verlinde, J., Korolev, A. V., Strapp, J. W., McFarquhar, G. M., Jackson, R., Brooks, S. D., Glen, A., and Wolde, M.: Toward ice formation closure in Arctic mixed-phase boundary layer clouds during ISDAC, *J. Geophys. Res. Atmos.*, 116, 0–08, <https://doi.org/10.1029/2011JD015910>, 2011.
- Baumgardner, D., Abel, S. J., Axisa, D., Cotton, R., Crosier, J., Field, P., Gurganus, C., Heymsfield, A., Korolev, A., Krämer, M., Lawson, P., McFarquhar, G., Ulanowski, Z., and Um, J.: Cloud Ice Properties: In Situ Measurement Challenges, *Meteorol. Monogr.*, 58, 9.1-9.23, <https://doi.org/10.1175/AMSMONOGRAPHS-D-16-0011.1>, 2017.
- Bühl, J., Seifert, P., Engelmann, R., and Ansmann, A.: Impact of vertical air motions on ice formation rate in mixed-phase cloud layers, *npj Clim. Atmos. Sci.*, 2, 36, <https://doi.org/10.1038/s41612-019-0092-6>, 2019.
- D'Alessandro, J. J., Diao, M., Wu, C., Liu, X., Jensen, J. B., and Stephens, B. B.: Cloud phase and relative humidity distributions over the Southern Ocean in austral summer based on in situ observations and CAM5 simulations, *J. Clim.*, 32, 2781–2805, <https://doi.org/10.1175/JCLI-D-18-0232.1>, 2019.
- D'Alessandro, J. J., McFarquhar, G. M., Wu, W., Stith, J. L., Jensen, J. B., and Rauber, R. M.: Characterizing the Occurrence and Spatial Heterogeneity of Liquid, Ice, and Mixed Phase Low-Level Clouds Over the Southern Ocean Using in Situ Observations Acquired During SOCRATES, *J. Geophys. Res. Atmos.*, 126, 1–18, <https://doi.org/10.1029/2020JD034482>, 2021.
- D'Alessandro, J. J., McFarquhar, G. M., Stith, J. L., Diao, M., DeMott, P. J., McCluskey, C. S., et al.: An evaluation of phase, aerosol-cloud interactions and microphysical properties of single- and multi-layer clouds over the Southern Ocean using in

- situ observations from SOCRATES. *Journal of Geophysical Research: Atmospheres*, 128, e2023JD038610. <https://doi.org/10.1029/2023JD038610>, 2023.
- 645 DeMott, P. J., Prenni, A. J., Liu, X., Kreidenweis, S. M., Petters, M. D., Twohy, C. H., Richardson, M. S., Eidhammer, T., and Rogers, D. C.: Predicting global atmospheric ice nuclei distributions and their impacts on climate. *Proc. Natl. Acad. Sci.*, 107, 11217–11222. <https://doi.org/10.1073/pnas.0910818107>, 2010.
- Desai, N., Diao, M., Shi, Y., Liu, X., and Silber, I.: Ship-based observations and climate model simulations of cloud phase  
650 over the Southern Ocean. *Journal of Geophysical Research: Atmospheres*, 128, e2023JD038581. <https://doi.org/10.1029/2023JD038581>, 2023.
- Diao, M., Jensen, J. B., Pan, L. L., Homeyer, C. R., Honomichl, S., Bresch, J. F., and Bansemer, A.: Distributions of ice supersaturation and ice crystals from airborne observations in relation to upper tropospheric dynamical boundaries. *J. Geophys. Res. Atmos.*, 120, 5101–5121. doi: 10.1002/2015JD023139, 2015.
- 655 Diao, M.: VCSEL 1Hz Water Vapor Data. <https://doi.org/10.26023/KFSD-Y8DQ-YCOD>, 2021.
- Fan, J., Ovtchinnikov, M., Comstock, J. M., McFarlane, S. A., and Khain, A.: Ice formation in Arctic mixed-phase clouds: Insights from a 3-D cloud-resolving model with size-resolved aerosol and cloud microphysics. *J. Geophys. Res.*, 114, <https://doi.org/10.1029/2008JD010782>, 2009.
- 660 Fan, J., Ghan, S., Ovtchinnikov, M., Liu, X., Rasch, P. J., and Korolev, A.: Representation of Arctic mixed-phase clouds and the Wegener-Bergeron-Findeisen process in climate models: Perspectives from a cloud-resolving study. *J. Geophys. Res. Atmos.*, 116. <https://doi.org/10.1029/2010JD015375>, 2011.
- Field, P. R., Hogan, R. J., Brown, P. R. A., Illingworth, A. J., Choullarton, T. W., Kaye, P. H., Hirst, E., and Greenaway, R.: Simultaneous radar and aircraft observations of mixed-phase cloud at the 100 m scale. *Q. J. R. Meteorol. Soc.*, 130, 1877–1904. <https://doi.org/10.1256/QJ.03.102>, 2004.
- 665 Field, P. R., Hill, A. A., Furtado, K., and Korolev, A.: Mixed-phase clouds in a turbulent environment. Part 2: Analytic treatment. *Q. J. R. Meteorol. Soc.*, 140, 870–880. <https://doi.org/10.1002/QJ.2175>, 2014.
- Hill, A. A., Field, P. R., Furtado, K., Korolev, A., and Shipway, B. J.: Mixed-phase clouds in a turbulent environment. Part 1: Large-eddy simulation experiments. *Q. J. R. Meteorol. Soc.*, 140, 855–869. <https://doi.org/10.1002/QJ.2177>, 2014.
- 670 Hobbs, P. V. and Rangno, A. L.: Ice Particle Concentrations in Clouds. *J. Atmos. Sci.*, 42, 2523–2549. [https://doi.org/10.1175/1520-0469\(1985\)042<2523:IPCIC>2.0.CO;2](https://doi.org/10.1175/1520-0469(1985)042<2523:IPCIC>2.0.CO;2), 1985.
- Hogan, R. J., Field, P. R., Illingworth, A. J., Cotton, R. J., and Choullarton, T. W.: Properties of embedded convection in warm-frontal mixed-phase cloud from aircraft and polarimetric radar. *Q. J. R. Meteorol. Soc.*, 128, 451–476. <https://doi.org/10.1256/003590002321042054>, 2002.
- Huang, Y., Chubb, T., Baumgardner, D., DeHoog, M., Siems, S. T., and Manton, M. J.: Evidence for secondary ice production in Southern Ocean open cellular convection. *Q. J. R. Meteorol. Soc.*, 143, 1685–1703. <https://doi.org/10.1002/qj.3041>, 2017.
- Hyder, P., Edwards, J. M., Allan, R. P., Hewitt, H. T., Bracegirdle, T. J., Gregory, J. M., Wood, R. A., Meijers, A. J. S., Mulcahy, J., Field, P., Furtado, K., Bodas-Salcedo, A., Williams, K. D., Copsey, D., Josey, S. A., Liu, C., Roberts, C. D.,

Sanchez, C., Ridley, J., Thorpe, L., Hardiman, S. C., Mayer, M., Berry, D. I., and Belcher, S. E.: Critical Southern Ocean climate model biases traced to atmospheric model cloud errors, *Nat. Commun.*, 9, 3625, <https://doi.org/10.1038/s41467-018-05634-2>, 2018.

680 Jackson, R. C., McFarquhar, G. M., Korolev, A. V., Earle, M. E., Liu, P. S. K., Lawson, R. P., Brooks, S., Wolde, M., Laskin, A., and Freer, M.: The dependence of ice microphysics on aerosol concentration in arctic mixed-phase stratus clouds during ISDAC and M-PACE, *J. Geophys. Res. Atmos.*, 117, 1–20, <https://doi.org/10.1029/2012JD017668>, 2012.

Järvinen, E., McCluskey, C. S., Waitz, F., Schnaiter, M., Bansemer, A., Bardeen, C. G., Gettelman, A., Heymsfield, A., Stith, J. L., Wu, W., D’Alessandro, J. J., McFarquhar, G. M., Diao, M., Finlon, J. A., Hill, T. C. J., Levin, E. J. T., Moore, K. A., and DeMott, P. J.: Evidence for Secondary Ice Production in Southern Ocean Maritime Boundary Layer Clouds, *J. Geophys. Res. Atmos.*, 127, 1–31, <https://doi.org/10.1029/2021JD036411>, 2022.

685 Korolev, A. V., Strapp, J. W., Isaac, G. A., and Nevzorov, A. N.: The Nevzorov Airborne Hot-Wire LWC–TWC Probe: Principle of Operation and Performance Characteristics, *J. Atmos. Ocean. Technol.*, 15, 1495–1510, [https://doi.org/10.1175/1520-0426\(1998\)015<1495:TNAHWL>2.0.CO;2](https://doi.org/10.1175/1520-0426(1998)015<1495:TNAHWL>2.0.CO;2), 1998.

690 Korolev, A. V., Isaac, G. A., Cober, S. G., Strapp, J. W., and Hallett, J.: Microphysical characterization of mixed-phase clouds, *Q. J. R. Meteorol. Soc.*, 129, 39–65, <https://doi.org/10.1256/qj.01.204>, 2003.

Korolev, A. V. and Mazin, I. P.: Supersaturation of water vapor in clouds, *J. Atmos. Sci.*, 60, 2957–2974, [https://doi.org/10.1175/1520-0469\(2003\)060<2957:SOWVIC>2.0.CO;2](https://doi.org/10.1175/1520-0469(2003)060<2957:SOWVIC>2.0.CO;2), 2003.

695 Korolev, A. V. and Isaac, G. A.: Relative Humidity in Liquid, Mixed-Phase, and Ice Clouds, *J. Atmos. Sci.*, 63, 2865–2880, <https://doi.org/10.1175/JAS3784.1>, 2006.

Korolev, A. V. and Field, P. R.: The Effect of Dynamics on Mixed-Phase Clouds: Theoretical Considerations, *J. Atmos. Sci.*, 65, 66–86, <https://doi.org/10.1175/2007JAS2355.1>, 2008.

700 Korolev, A. V., Emery, E. F., Strapp, J. W., Cober, S. G., and Isaac, G. A.: Quantification of the effects of shattering on airborne ice particle measurements, *J. Atmos. Ocean. Technol.*, 30, 2527–2553, <https://doi.org/10.1175/JTECH-D-13-00115.1>, 2013.

Korolev, A. V., McFarquhar, G., Field, P. R., Franklin, C., Lawson, P., Wang, Z., Williams, E., Abel, S. J., Axisa, D., Borrmann, S., Crosier, J., Fugal, J., Krämer, M., Lohmann, U., Schlenker, O., Schnaiter, M., and Wendisch, M.: Mixed-Phase Clouds: Progress and Challenges, *Meteorol. Monogr.*, 58, 5.1-5.50, <https://doi.org/10.1175/AMSMONOGRAPHIS-D-17-0001.1>, 2017.

705 Korolev, A. V. and Milbrandt, J.: How Are Mixed-Phase Clouds Mixed?, *Geophys. Res. Lett.*, 49, 1–7, <https://doi.org/10.1029/2022GL099578>, 2022.

Matus, A. V. and L’Ecuyer, T. S.: The role of cloud phase in Earth’s radiation budget, *J. Geophys. Res. Atmos.*, 122, 2559–2578, <https://doi.org/10.1002/2016JD025951>, 2017.

710 McCluskey, C. S., Hill, T. C. J., Humphries, R. S., Rauker, A. M., Moreau, S., Stratton, P. G., Chambers, S. D., Williams, A. G., McRobert, I., Ward, J., Keywood, M. D., Harnwell, J., Ponsonby, W., Loh, Z. M., Krummel, P. B., Protat, A., Kreidenweis,

S. M., and DeMott, P. J.: Observations of Ice Nucleating Particles Over Southern Ocean Waters, *Geophys. Res. Lett.*, 45, 11,989–11,997, <https://doi.org/10.1029/2018GL079981>, 2018.

715 [McFarquhar, G. M., Bretherton, C. S., Marchand, R., Protat, A., DeMott, P. J., Alexander, S. P., Roberts, G. C., Twohy, C. H., Toohey, D., Siems, S., Huang, Y., Wood, R., Rauber, R. M., Lasher-Trapp, S., Jensen, J., Stith, J. L., Mace, J., Um, J., Järvinen, E., Schnaiter, M., Gettelman, A., Sanchez, K. J., McCluskey, C. S., Russell, L. M., McCoy, I. L., Atlas, R. L., Bardeen, C. G., Moore, K. A., Hill, T. C. J., Humphries, R. S., Keywood, M. D., Ristovski, Z., Cravigan, L., Schofield, R., Fairall, C., Mallet, M. D., Kreidenweis, S. M., Rainwater, B., D’Alessandro, J., Wang, Y., Wu, W., Saliba, G., Levin, E. J. T., Ding, S., Lang, F., Truong, S. C. H., Wolff, C., Haggerty, J., Harvey, M. J., Klekociuk, A. R., and McDonald, A.: Observations of Clouds, Aerosols, Precipitation, and Surface Radiation over the Southern Ocean: An Overview of CAPRICORN, MARCUS, MICRE, and SOCRATES, \*Bull. Am. Meteorol. Soc.\*, 102, E894–E928, <https://doi.org/10.1175/BAMS-D-20-0132.1>, 2021.](#)

720 [Mohrmann, J., et al. 2021. University of Washington Ice-Liquid Discriminator single particle phase classifications and 1 Hz particle size distributions/heterogeneity estimate. Version 1.0. UCAR/NCAR— Earth Observing Laboratory, <https://doi.org/10.26023/PA5W-4DRX-W50A>. Accessed 21 Aug 2022.](#)

725 [Morrison, H., de Boer, G., Feingold, G., Harrington, J., Shupe, M. D., and Sulia, K.: Resilience of persistent Arctic mixed-phase clouds, \*Nat. Geosci.\*, 5, 11–17, <https://doi.org/10.1038/ngeo1332>, 2012.](#)

[Moss, S. J. and Johnson, D. W.: Aircraft measurements to validate and improve numerical model parametrisations of ice to water ratios in clouds, \*Atmos. Res.\*, 34, 1–25, \[https://doi.org/10.1016/0169-8095\\(94\\)90078-7\]\(https://doi.org/10.1016/0169-8095\(94\)90078-7\), 1994.](#)

[Murphy, D. M. and Koop, T.: Review of the vapour pressures of ice and supercooled water for atmospheric applications, \*Q. J. R. Meteorol. Soc.\*, 131, 1539–1565, <https://doi.org/10.1256/qj.04.94>, 2005.](#)

730 [Norgren, M. S., de Boer, G., and Shupe, M. D.: Observed aerosol suppression of cloud ice in low-level Arctic mixed-phase clouds, \*Atmos. Chem. Phys.\*, 18, 13345–13361, <https://doi.org/10.5194/acp-18-13345-2018>, 2018.](#)

[Pinto, J. O.: Autumnal mixed-phase cloudy boundary layers in the arctic, \*J. Atmos. Sci.\*, 55, 2016–2038, \[https://doi.org/10.1175/1520-0469\\(1998\\)055<2016:AMPCBL>2.0.CO;2\]\(https://doi.org/10.1175/1520-0469\(1998\)055<2016:AMPCBL>2.0.CO;2\), 1998.](#)

735 [Qiu, S., Xi, B., and Dong, X.: Influence of Wind Direction on Thermodynamic Properties and Arctic Mixed-Phase Clouds in Autumn at Utqiaġvik, Alaska, \*J. Geophys. Res. Atmos.\*, 123, 9589–9603, <https://doi.org/10.1029/2018JD028631>, 2018.](#)

[Rauber, R. M. and Tokay, A.: An Explanation for the Existence of Supercooled Water at the Top of Cold Clouds, \*J. Atmos. Sci.\*, 48, 1005–1023, \[https://doi.org/10.1175/1520-0469\\(1991\\)048<1005:AEFTEO>2.0.CO;2\]\(https://doi.org/10.1175/1520-0469\(1991\)048<1005:AEFTEO>2.0.CO;2\), 1991.](#)

740 [Romatschke, U., and Vivekanandan, J.: Cloud and precipitation particle identification using cloud radar and lidar measurements: Retrieval technique and validation. \*Earth and Space Science\*, 9, e2022EA002299, <https://doi.org/10.1029/2022EA002299>, 2022.](#)

[Shupe, M. D., Kollias, P., Persson, P. O. G., and McFarquhar, G. M.: Vertical Motions in Arctic Mixed-Phase Stratiform Clouds, \*J. Atmos. Sci.\*, 65, 1304–1322, <https://doi.org/10.1175/2007JAS2479.1>, 2008.](#)

745 [Smith, A. J., Larson, V. E., Niu, J., Kankiewicz, J. A., and Carey, L. D.: Processes that generate and deplete liquid water and snow in thin midlevel mixed-phase clouds, \*J. Geophys. Res. Atmos.\*, 114, 1–18, <https://doi.org/10.1029/2008JD011531>, 2009.](#)

Storelvmo, T.: Aerosol Effects on Climate via Mixed-Phase and Ice Clouds, *Annu. Rev. Earth Planet. Sci.*, 45, 199–222, <https://doi.org/10.1146/annurev-earth-060115-012240>, 2017.

Tan, I. and Storelvmo, T.: Sensitivity Study on the Influence of Cloud Microphysical Parameters on Mixed-Phase Cloud Thermodynamic Phase Partitioning in CAM5, *J. Atmos. Sci.*, 73, 709–728, <https://doi.org/10.1175/JAS-D-15-0152.1>, 2016.

750 Tan, I., Storelvmo, T., and Zelinka, M. D.: Observational constraints on mixed-phase clouds imply higher climate sensitivity, *Science* (80-. ), 352, 224–227, <https://doi.org/10.1126/science.aad5300>, 2016.

Wallace, J. M. and Hobbs, P. V.: *Atmospheric Science: An Introductory Survey*, New York, USA, <https://doi.org/10.1016/C2009-0-00034-8>, 1977.

Wang, Z., and Coauthors: Single Aircraft Integration of Remote Sensing and In Situ Sampling for the Study of Cloud Microphysics and Dynamics, *Bull. Amer. Meteor. Soc.*, 93, 653–668, <https://doi.org/10.1175/BAMS-D-11-00044.1>, 2012.

755 Wang, Y., McFarquhar, G. M., Rauber, R. M., Zhao, C., Wu, W., Finlon, J. A., Stechman, D. M., Stith, J., Jensen, J. B., Schnaiter, M., Järvinen, E., Waitz, F., Vivekanandan, J., Dixon, M., Rainwater, B., and Toohey, D. W.: Microphysical Properties of Generating Cells Over the Southern Ocean: Results From SOCRATES, *J. Geophys. Res. Atmos.*, 125, 1–23, <https://doi.org/10.1029/2019JD032237>, 2020.

760 Westbrook, C. D. and Illingworth, A. J.: Evidence that ice forms primarily in supercooled liquid clouds at temperatures >-27°C, *Geophys. Res. Lett.*, 38, 1–4, <https://doi.org/10.1029/2011GL048021>, 2011.

Wood, R., and Field, P. R.: The Distribution of Cloud Horizontal Sizes, *J. Climate*, 24, 4800–4816, <https://doi.org/10.1175/2011JCLI4056.1>, 2011.

765 Wu, W., and McFarquhar, G. M.: On the impacts of different definitions of maximum dimension for nonspherical particles recorded by 2D imaging probes, *Journal of Atmospheric and Oceanic Technology*, 33(5), 1057–1072, <https://doi.org/10.1175/JTECH-D-15-0177.1>, 2016.

Yang, C. A., Diao, M., Gettelman, A., Zhang, K., Sun, J., McFarquhar, G., and Wu, W.: Ice and Supercooled Liquid Water Distributions Over the Southern Ocean Based on In Situ Observations and Climate Model Simulations, *J. Geophys. Res. Atmos.*, 126, <https://doi.org/10.1029/2021JD036045>, 2021.

770 Yip, J., Diao, M., Silber, I., and Gettelman, A.: Evaluation of the CAM6 Climate Model Using Cloud Observations at McMurdo Station, Antarctica, *J. Geophys. Res.— Atmos.*, 126, 1–21, <https://doi.org/10.1029/2021JD034653>, 2021.

Zaremba, T. J., Rauber, R. M., McFarquhar, G. M., Hayman, M., Finlon, J. A., and Stechman, D. M.: Phase Characterization of Cold Sector Southern Ocean Cloud Tops: Results From SOCRATES, *J. Geophys. Res. Atmos.*, 125, <https://doi.org/10.1029/2020JD033673>, 2020.

775 Zhang, M., Liu, X., Diao, M., D’Alessandro, J. J., Wang, Y., Wu, C., Zhang, D., Wang, Z., and Xie, S.: Impacts of Representing Heterogeneous Distribution of Cloud Liquid and Ice on Phase Partitioning of Arctic Mixed-Phase Clouds with NCAR CAM5, *J. Geophys. Res. Atmos.*, 124, 13071–13090, <https://doi.org/10.1029/2019JD030502>, 2019.

Zhao, X. and Liu, X.: Global Importance of Secondary Ice Production, *Geophys. Res. Lett.*, 48, 1–11, <https://doi.org/10.1029/2021GL092581>, 2021.



- 780 Zhao, X., Liu, X., Burrows, S., DeMott, P. J., Diao, M., McFarquhar, G. M., et al. Important ice processes are missed by the Community Earth System Model in Southern Ocean mixed-phase clouds: Bridging SOCRATES observations to model developments. *Journal of Geophysical Research: Atmospheres*, 128, e2022JD037513. <https://doi.org/10.1029/2022JD037513>, 2023.
- 785 Atlas, R., Mohrmann, J., Finlon, J., Lu, J., Hsiao, I., Wood, R., and Diao, M.: The University of Washington Ice–Liquid Discriminator (UWILD) improves single-particle phase classifications of hydrometeors within Southern Ocean clouds using machine learning, *Atmos. Meas. Tech.*, 14, 7079–7101, <https://doi.org/10.5194/amt-14-7079-2021>, 2021.
- Bühl, J., Seifert, P., Engelmann, R., and Ansmann, A.: Impact of vertical air motions on ice formation rate in mixed-phase cloud layers, *npj Clim. Atmos. Sci.*, 2, 36, <https://doi.org/10.1038/s41612-019-0092-6>, 2019.
- 790 D'Alessandro, J. J., Diao, M., Wu, C., Liu, X., Jensen, J. B., and Stephens, B. B.: Cloud phase and relative humidity distributions over the Southern Ocean in austral summer based on in-situ observations and CAM5 simulations, *J. Clim.*, 32, <https://doi.org/10.1175/JCLI-D-18-0232.1>, 2019.
- D'Alessandro, J. J., McFarquhar, G. M., Wu, W., Stith, J. L., Jensen, J. B., and Rauber, R. M.: Characterizing the Occurrence and Spatial Heterogeneity of Liquid, Ice, and Mixed-Phase Low-Level Clouds Over the Southern Ocean Using in-Situ Observations—Acquired During SOCRATES, *J. Geophys. Res. Atmos.*, 126, e2020JD034482, <https://doi.org/https://doi.org/10.1029/2020JD034482>, 2021.
- 795 DeMott, P. J., Prenni, A. J., Liu, X., Kreidenweis, S. M., Petters, M. D., Twohy, C. H., Richardson, M. S., Eidhammer, T., and Rogers, D. C.: Predicting global atmospheric ice nuclei distributions and their impacts on climate, *Proc. Natl. Acad. Sci.*, 107, 11217–11222, <https://doi.org/10.1073/pnas.0910818107>, 2010.
- 800 Diao, M.: VCSEL 1Hz Water Vapor Data, <https://doi.org/10.26023/KFSD-Y8DQ-YC0D>, 2021.
- Huang, Y., Chubb, T., Baumgardner, D., DeHoog, M., Siems, S. T., and Manton, M. J.: Evidence for secondary ice production in Southern Ocean open cellular convection, *Q. J. R. Meteorol. Soc.*, 143, 1685–1703, <https://doi.org/10.1002/qj.3041>, 2017.
- Hyder, P., Edwards, J. M., Allan, R. P., Hewitt, H. T., Bracegirdle, T. J., Gregory, J. M., Wood, R. A., Meijers, A. J. S., Muleahy, J., Field, P., Furtado, K., Bodas-Saleedo, A., Williams, K. D., Copsey, D., Josey, S. A., Liu, C., Roberts, C. D., Sanchez, C., Ridley, J., Thorpe, L., Hardiman, S. C., Mayer, M., Berry, D. I., and Belcher, S. E.: Critical Southern Ocean climate model biases traced to atmospheric model cloud errors, *Nat. Commun.*, 9, 3625, <https://doi.org/10.1038/s41467-018-05634-2>, 2018.
- 805 Jackson, R. C., McFarquhar, G. M., Korolev, A. V., Earle, M. E., Liu, P. S. K., Lawson, R. P., Brooks, S., Wolde, M., Laskin, A., and Freer, M.: The dependence of ice microphysics on aerosol concentration in arctic mixed-phase stratus clouds during ISDAC and M-PACE, *J. Geophys. Res. Atmos.*, 117, <https://doi.org/https://doi.org/10.1029/2012JD017668>, 2012.
- Järvinen, E., McCluskey, C. S., Waitz, F., Schnaiter, M., Bansemmer, A., Bardeen, C. G., Gettelman, A., Heymsfield, A., Stith, J. L., Wu, W., D'Alessandro, J. J., McFarquhar, G. M., Diao, M., Finlon, J. A., Hill, T. C. J., Levin, E. J. T., Moore, K. A., and DeMott, P. J.: Evidence for Secondary Ice Production in Southern Ocean Maritime Boundary Layer Clouds, *J. Geophys.*

- Res. Atmos., 127, <https://doi.org/10.1029/2021JD036411>, 2022.
- 815 Korolev, A., Isaac, G. A., Cober, S. G., Strapp, J. W., and Hallett, J.: Microphysical characterization of mixed phase clouds, *Q. J. R. Meteorol. Soc.*, 129, 39–65, <https://doi.org/https://doi.org/10.1256/qj.01.204>, 2003.
- Korolev, A. V. and Field, P. R.: The Effect of Dynamics on Mixed-Phase Clouds: Theoretical Considerations, *J. Atmos. Sci.*, 65, 66–86, <https://doi.org/10.1175/2007JAS2355.1>, 2008.
- 820 Korolev, A. V., Strapp, J. W., Isaac, G. A., and Nevzorov, A. N.: The Nevzorov Airborne Hot-Wire LWC-TWC Probe: Principle of Operation and Performance Characteristics, *J. Atmos. Ocean. Technol.*, 15, 1495–1510, [https://doi.org/10.1175/1520-0426\(1998\)015<1495:TNAHWL>2.0.CO;2](https://doi.org/10.1175/1520-0426(1998)015<1495:TNAHWL>2.0.CO;2), 1998.
- Korolev, A., McFarquhar, G., Field, P. R., Franklin, C., Lawson, P., Wang, Z., Williams, E., Abel, S. J., Axisa, D., Borrmann, S., Crosier, J., Fugal, J., Krämer, M., Lohmann, U., Schlenzcek, O., Schnaiter, M., and Wendisch, M.: Mixed-Phase Clouds: Progress and Challenges, *Meteorol. Monogr.*, 58, 5.1–5.50, <https://doi.org/10.1175/AMSMONOGRAPHIS-D-17-0001.1>, 2017.
- 825 Matus, A. V. and L'Euuyer, T. S.: The role of cloud phase in Earth's radiation budget, *J. Geophys. Res. Atmos.*, 122, 2559–2578, <https://doi.org/https://doi.org/10.1002/2016JD025951>, 2017.
- McCluskey, C. S., Hill, T. C. J., Humphries, R. S., Rauker, A. M., Moreau, S., Strutton, P. G., Chambers, S. D., Williams, A. G., McRobert, I., Ward, J., Keywood, M. D., Harnwell, J., Ponsonby, W., Loh, Z. M., Krummel, P. B., Protat, A., Kreidenweis, S. M., and DeMott, P. J.: Observations of Ice-Nucleating Particles Over Southern Ocean Waters, *Geophys. Res. Lett.*, 45, 11,989–11,997, <https://doi.org/10.1029/2018GL079981>, 2018.
- 830 McFarquhar, G. M., Bretherton, C. S., Marchand, R., Protat, A., DeMott, P. J., Alexander, S. P., Roberts, G. C., Twohy, C. H., Toohey, D., Siems, S., Huang, Y., Wood, R., Rauber, R. M., Lasher-Trapp, S., Jensen, J., Stith, J. L., Mace, J., Um, J., Järvinen, E., Schnaiter, M., Gettelman, A., Sanchez, K. J., McCluskey, C. S., Russell, L. M., McCoy, I. L., Atlas, R. L., Bardeen, C. G., Moore, K. A., Hill, T. C. J., Humphries, R. S., Keywood, M. D., Ristovski, Z., Cravigan, L., Schofield, R.,
- 835 Fairall, C., Mallet, M. D., Kreidenweis, S. M., Rainwater, B., D'Alessandro, J., Wang, Y., Wu, W., Saliba, G., Levin, E. J. T., Ding, S., Lang, F., Truong, S. C. H., Wolff, C., Haggerty, J., Harvey, M. J., Klekociuk, A. R., and McDonald, A.: Observations of Clouds, Aerosols, Precipitation, and Surface Radiation over the Southern Ocean: An Overview of CAPRICORN, MARCUS, MICRE, and SOCRATES, *Bull. Am. Meteorol. Soc.*, 102, E894–E928, <https://doi.org/10.1175/BAMS-D-20-0132.1>, 2021.
- Mohrmann, J., et al. 2021. University of Washington Ice-Liquid Discriminator single-particle-phase-classifications and 1-Hz particle-size-distributions/heterogeneity-estimate. Version 1.0. UCAR/NCAR—Earth Observing Laboratory. <https://doi.org/10.26023/PA5W-4DRX-W50A>. Accessed 21-Aug-2022.
- 840 Morrison, H., de Boer, G., Feingold, G., Harrington, J., Shupe, M. D., and Sulia, K.: Resilience of persistent Arctic mixed-phase clouds, *Nat. Geosci.*, 5, 11–17, <https://doi.org/10.1038/ngeo1332>, 2012.
- Murphy, D. M. and Koop, T.: Review of the vapour pressures of ice and supercooled water for atmospheric applications, *Q. J. R. Meteorol. Soc.*, 131, 1539–1565, <https://doi.org/10.1256/qj.04.94>, 2005.
- 845 Norgren, M. S., de Boer, G., and Shupe, M. D.: Observed aerosol suppression of cloud ice in low-level Arctic mixed-phase clouds, *Atmos. Chem. Phys.*, 18, 13345–13361, <https://doi.org/10.5194/acp-18-13345-2018>, 2018.

- Qiu, S., Xi, B., and Dong, X.: Influence of Wind Direction on Thermodynamic Properties and Arctic Mixed-Phase Clouds in Autumn at Utqiagvik, Alaska, *J. Geophys. Res. Atmos.*, 123, 9589–9603, <https://doi.org/https://doi.org/10.1029/2018JD028631>, 2018.
- 850 Shupe, M. D., Kollias, P., Persson, P. O. G., and McFarquhar, G. M.: Vertical Motions in Arctic Mixed-Phase Stratiform Clouds, *J. Atmos. Sci.*, 65, 1304–1322, <https://doi.org/10.1175/2007JAS2479.1>, 2008.
- Storelvmo, T.: Aerosol Effects on Climate via Mixed-Phase and Ice Clouds, *Annu. Rev. Earth Planet. Sci.*, 45, 199–222, <https://doi.org/10.1146/annurev-earth-060115-012240>, 2017.
- 855 Tan, I., Storelvmo, T., and Zelinka, M. D.: Observational constraints on mixed-phase clouds imply higher climate sensitivity, *Science (80-)*, 352, 224–227, <https://doi.org/10.1126/science.aad5300>, 2016.
- Tan, I. and Storelvmo, T.: Sensitivity Study on the Influence of Cloud Microphysical Parameters on Mixed-Phase Cloud Thermodynamic Phase Partitioning in CAM5, *J. Atmos. Sci.*, 73, 709–728, <https://doi.org/10.1175/JAS-D-15-0152.1>, 2016.
- Wang, Y., McFarquhar, G. M., Rauber, R. M., Zhao, C., Wu, W., Finlon, J. A., Stechman, D. M., Stith, J., Jensen, J. B., 860 Schnaiter, M., Järvinen, E., Waitz, F., Vivekanandan, J., Dixon, M., Rainwater, B., and Toohey, D. W.: Microphysical Properties of Generating Cells Over the Southern Ocean: Results From SOCRATES, *J. Geophys. Res. Atmos.*, 125, e2019JD032237, <https://doi.org/https://doi.org/10.1029/2019JD032237>, 2020.
- Yang, C. A., Diao, M., Gettelman, A., Zhang, K., Sun, J., McFarquhar, G., and Wu, W.: Ice and Supercooled Liquid Water Distributions Over the Southern Ocean Based on In Situ Observations and Climate Model Simulations, *J. Geophys. Res. Atmos.*, 126, <https://doi.org/10.1029/2021JD036045>, 2021.
- 865 Yip, J., Diao, M., Silber, I., and Gettelman, A.: Evaluation of the CAM6 Climate Model Using Cloud Observations at McMurdo Station, Antarctica, *J. Geophys. Res. Atmos.*, 126, e2021JD034653, <https://doi.org/10.1029/2021JD034653>, 2021.
- Zaremba, T. J., Rauber, R. M., McFarquhar, G. M., Hayman, M., Finlon, J. A., and Stechman, D. M.: Phase Characterization of Cold Sector Southern Ocean Cloud Tops: Results From SOCRATES, *J. Geophys. Res. Atmos.*, 125, e2020JD033673, <https://doi.org/https://doi.org/10.1029/2020JD033673>, 2020.
- 870 Zhang, M., Liu, X., Diao, M., D'Alessandro, J. J., Wang, Y., Wu, C., Zhang, D., Wang, Z., and Xie, S.: Impacts of Representing Heterogeneous Distribution of Cloud Liquid and Ice on Phase Partitioning of Arctic Mixed-Phase Clouds with NCAR CAM5, *J. Geophys. Res. Atmos.*, 124, 13071–13090, <https://doi.org/10.1029/2019JD030502>, 2019.
- Zhao, X. and Liu, X.: Global Importance of Secondary Ice Production, *Geophys. Res. Lett.*, 48, <https://doi.org/10.1029/2021GL092581>, 2021.
- 875

**Table 1.** Definitions of four transition phases of mixed-phase clouds, alongside their required spatial ratios of LCR, ICR, and MCR.

Phase	Description	Number of seconds	Number of TCRs	Liquid Spatial Ratio of LCR	Ice Spatial Ratio of ICR	Mixed Spatial Ratio of MCR
				M1 = length of LCR / total segment length	M2 = length of ICR / total segment length	M3 = length of MCR / total segment length
1	Only LCR	8243	1163	M1 = 1	M2 = 0	M3 = 0
2	MCR appears	12557 (LCR: 11096, MCR: 1461)	142	$0 < M1 < 10$	M2 = 0	$0 < M3 \leq 1$
3	Pure ICR must appear	11988 (LCR: 3478, MCR: 2973, ICR: 5537)	249	$0 \leq M1 < 1$	$0 < M2 < 1$	$0 \leq M3 < 1$
4	Only ICR	8646	1193	M1 = 0	M2 = 1	M3 = 0

- Formatted: Indent: Left: 0.06"
- Formatted: Indent: Left: 0.08"
- Formatted Table
- Formatted: Font: Bold
- Formatted: Centered
- Formatted: Centered
- Formatted: Centered
- Formatted: Centered
- Formatted: Centered

880

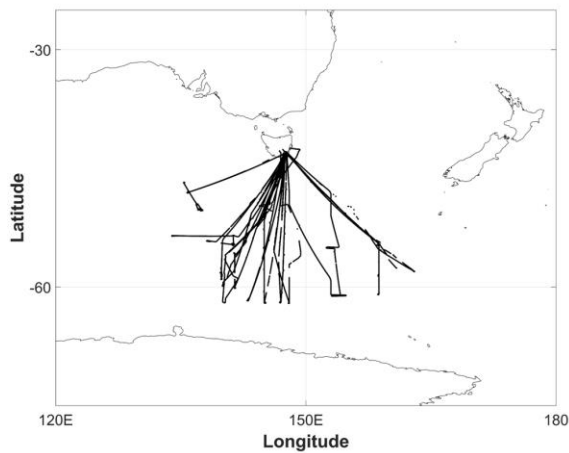
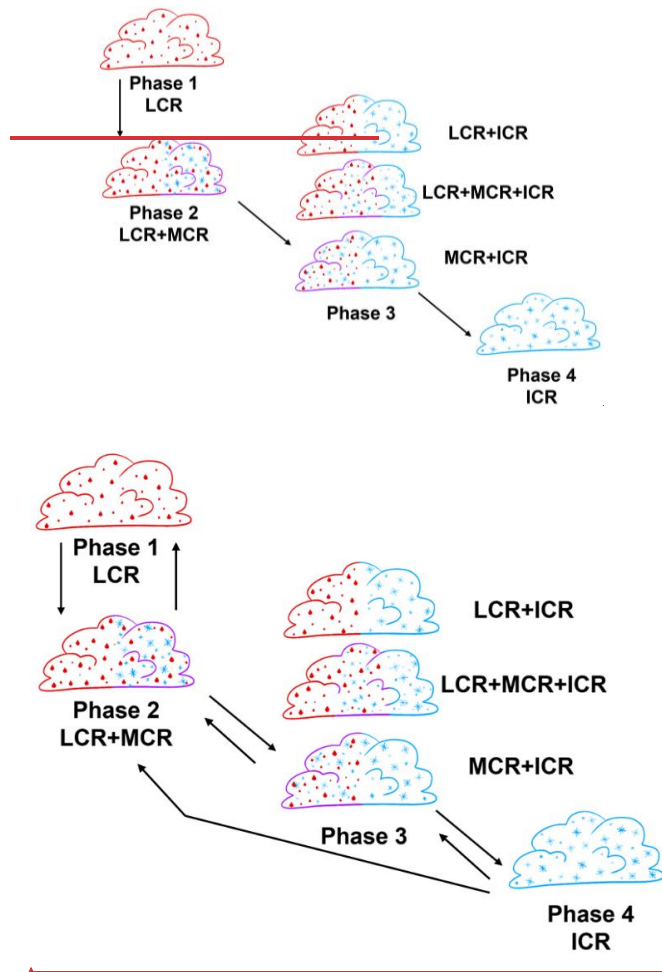


**Figure 1.** Map of the flight tracks for SOCRATES for only temperatures between 0°C and -40°C.



Formatted: Font: 10 pt

885 **Figure 2.** A conceptual and idealized diagram of the four transition phases for the phase exchange between supercooled liquid water and ice particles in mixed-phase clouds evolution. Red, blue, and purple shading indicates liquid cloud region (LCR), ice cloud region (ICR) and mixed cloud region (MCR), respectively.

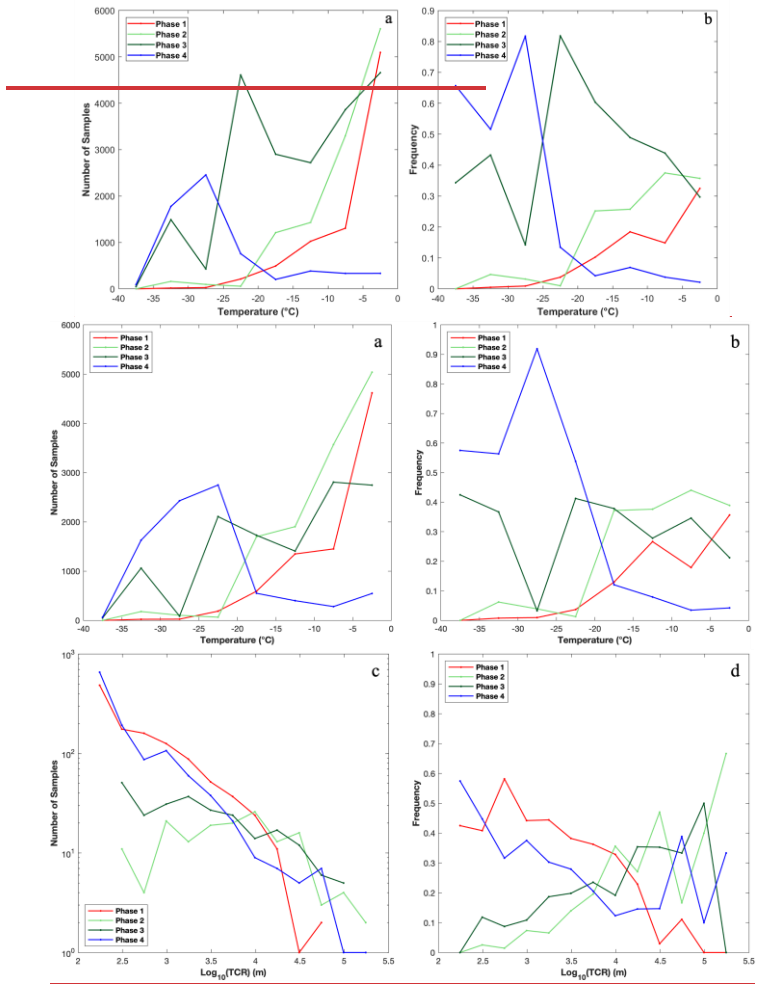


**Figure 3. Distributions of four transition phases at various temperatures. (a) Number of samples and (b) probability of each phase. The probability is normalized by the number of samples of all phases in each 5-degree temperature bin.**

**Figure 3.** Distributions of four transition phases at various temperatures in terms of (a) number of 1-Hz samples and (b) frequency of each phase. In (b), the frequency of each phase is normalized by the number of samples of all phases in each 5-degree temperature bin. (c) Number of 1-Hz samples and (d) frequency distribution of TCR lengths in logarithmic scale. In (d), frequency is calculated as the number of 1-Hz samples of a specific phase divided by the total number of 1-Hz in-cloud samples in each  $10^{0.25}$  bin.

**Formatted:** Font: 10 pt, Bold

**Formatted:** Font: 10 pt

**Formatted:** Font: 10 pt

**Formatted:** Font: 10 pt

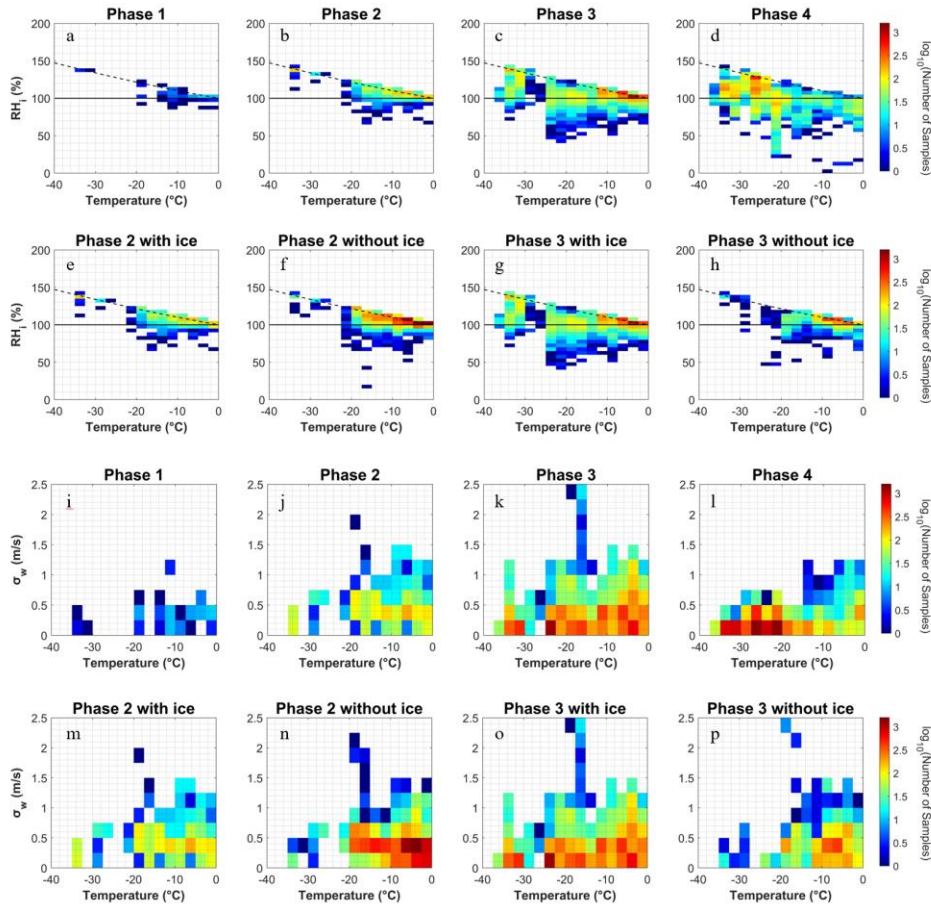


Figure 4. Distributions of (a-h)  $RH_1$  and (i-p)  $\sigma_w$  in various transition phases as a function of temperature. Dashed lines in (a) – (h) indicate liquid saturation.

Formatted: Font: Not Bold

Formatted: Font: Not Bold

Formatted: Font: Not Bold, Subscript

Formatted: Font: Not Bold

Formatted: Subscript



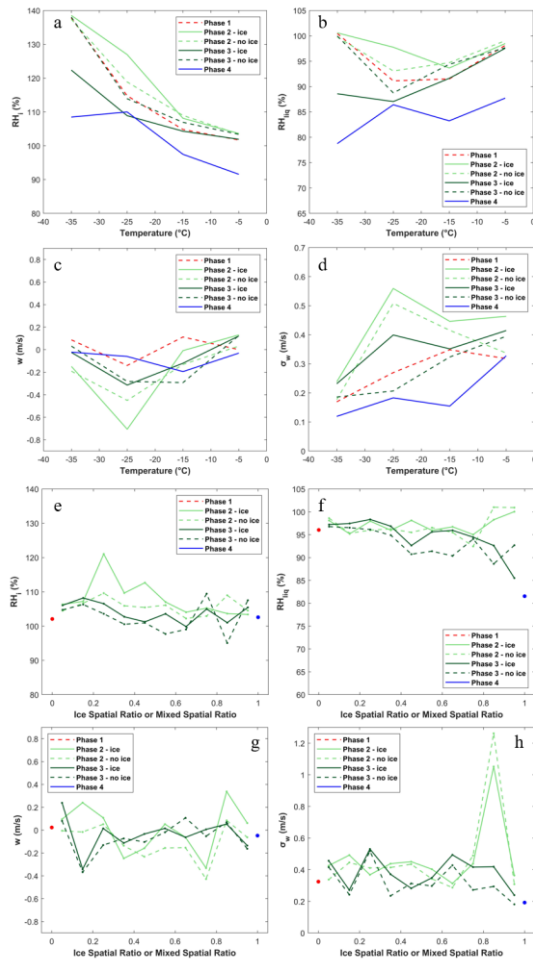


**Figure 510.** Distributions of (a)  $RH_i$ , (b)  $RH_{ice}$ , (c) vertical velocity ( $w$ ), and (d) standard deviation of vertical velocity ( $\sigma_w$ ) for various transition phases at different temperatures. (e-h) Similar to (a-d), but in relation to various mixed spatial ratios or ice spatial ratios. Phases 1 and 4 show ice spatial ratio at 0 and 1, respectively, and therefore only a single dot is shown for phases 1 and 4 in (e-h).

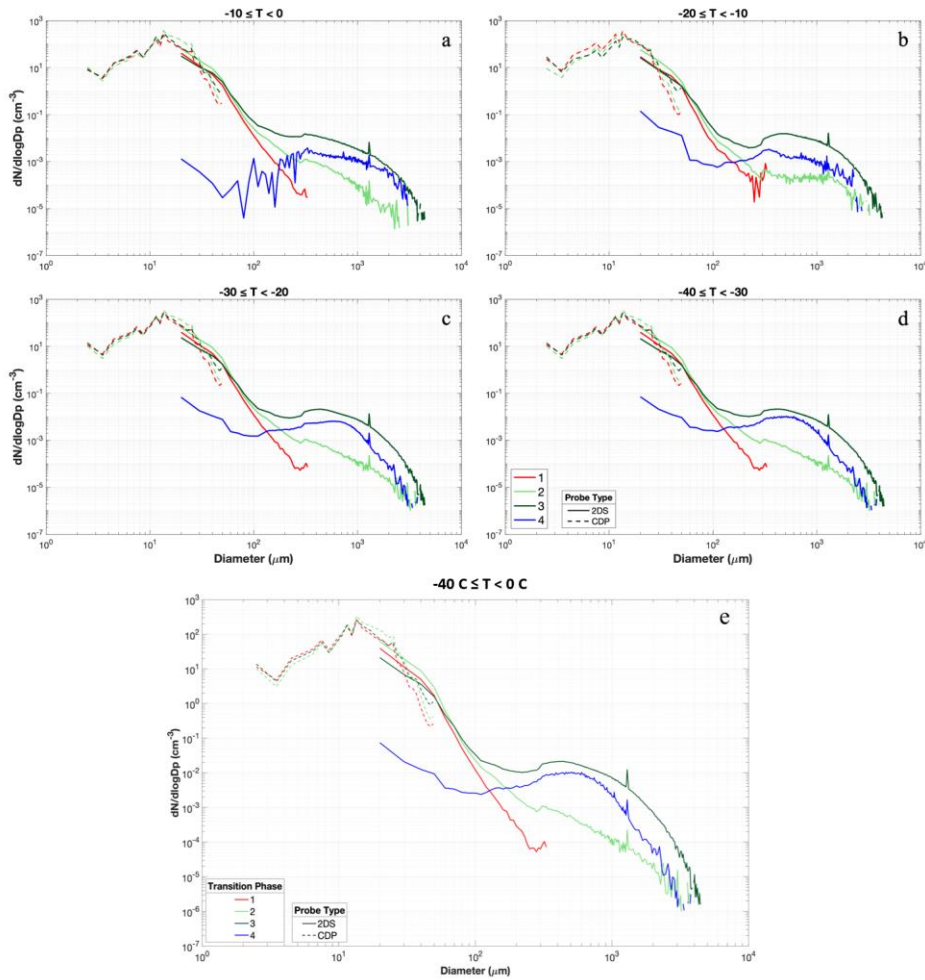


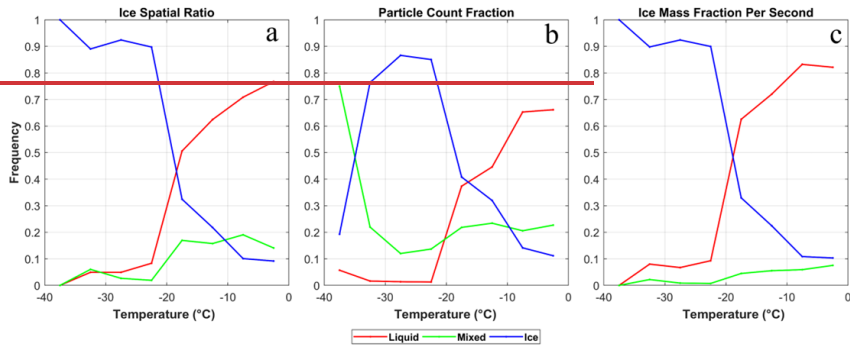
**Figure 65.** Particle size distribution of the four transition phases for mixed-phase clouds separated by probe types and temperature ranges. Phase 4 only shows 2DS measurements because ice particles measured by CDP are excluded from the analysis.

Formatted: Font: 9 pt, Not Bold

Formatted: Centered

Formatted: Font: 10 pt

Formatted: Font: 10 pt



920 **Figure 4.** Cloud phase occurrence frequencies at various temperatures. Cloud phase identification methods based on (a) ice spatial ratio for an entire in-cloud segment, (b) ice particle number fraction per second, and (c) ice mass fraction per second.

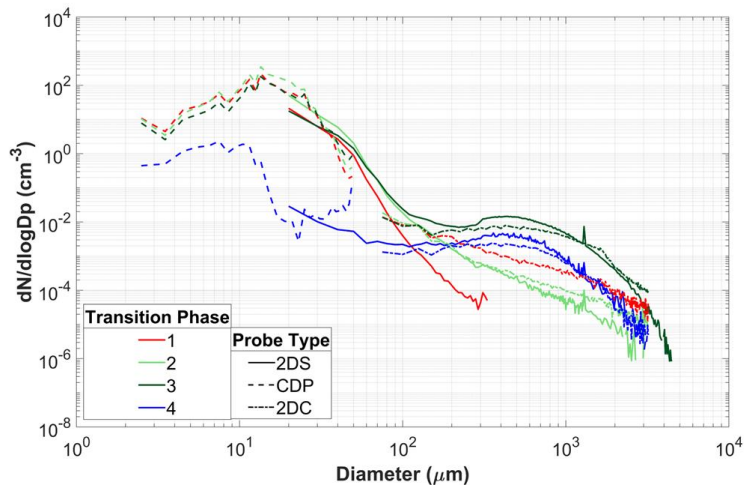


Figure 5. Particle size distribution of the four transition phases for mixed-phase clouds separated by probe type.

Formatted: Centered, Space After: 10 pt

925

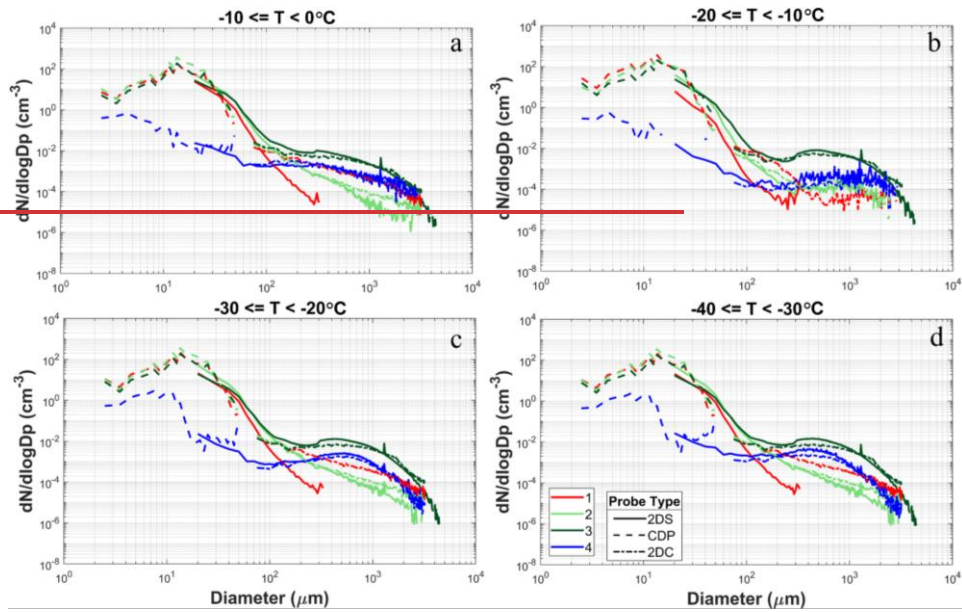
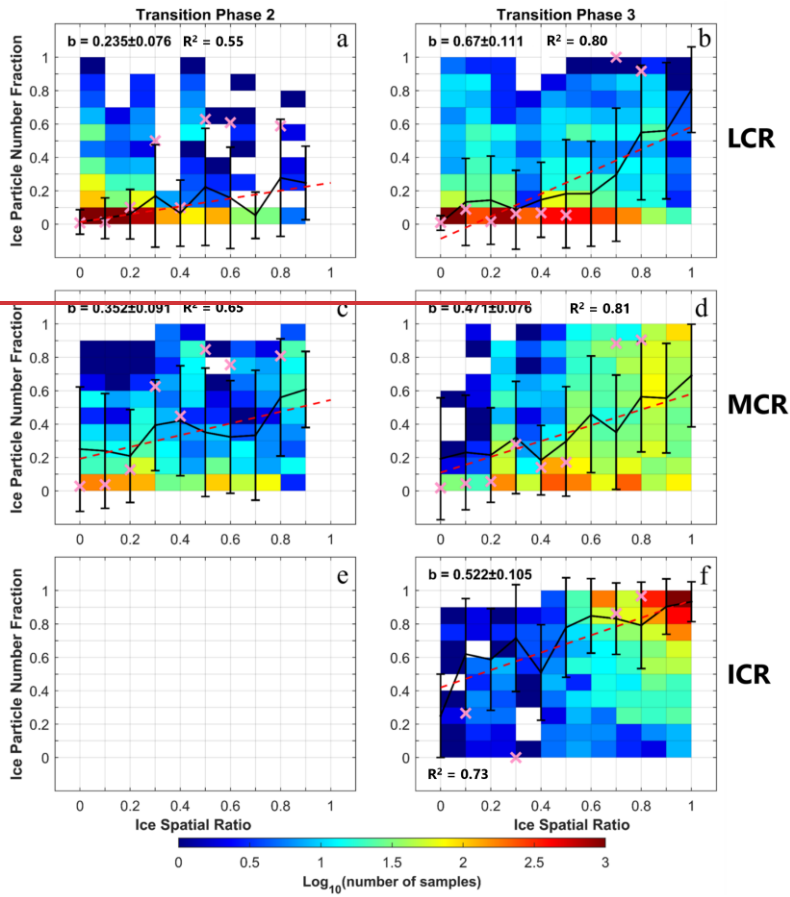
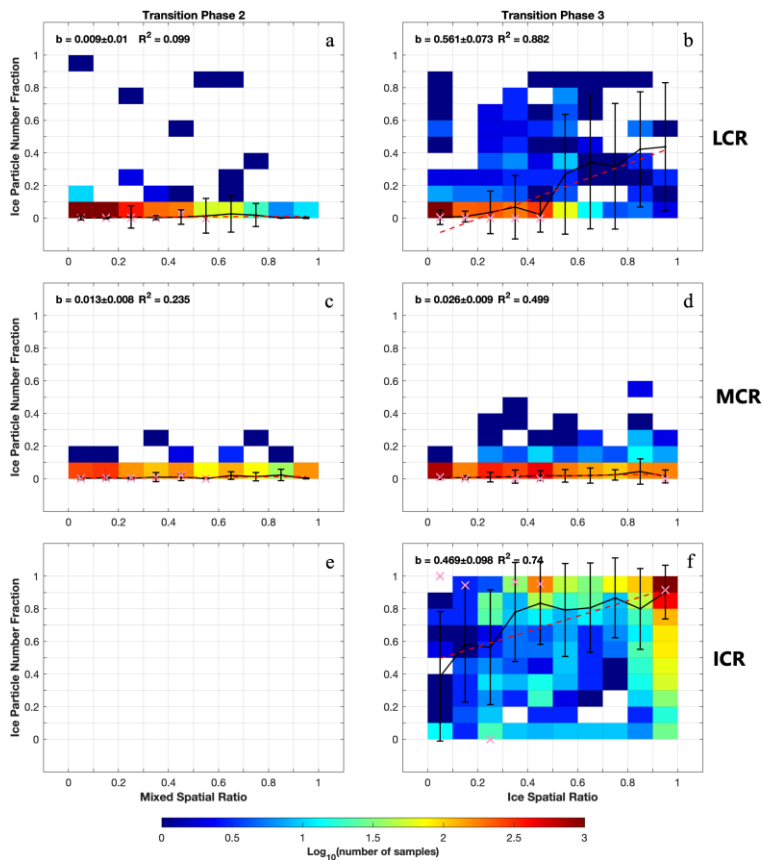


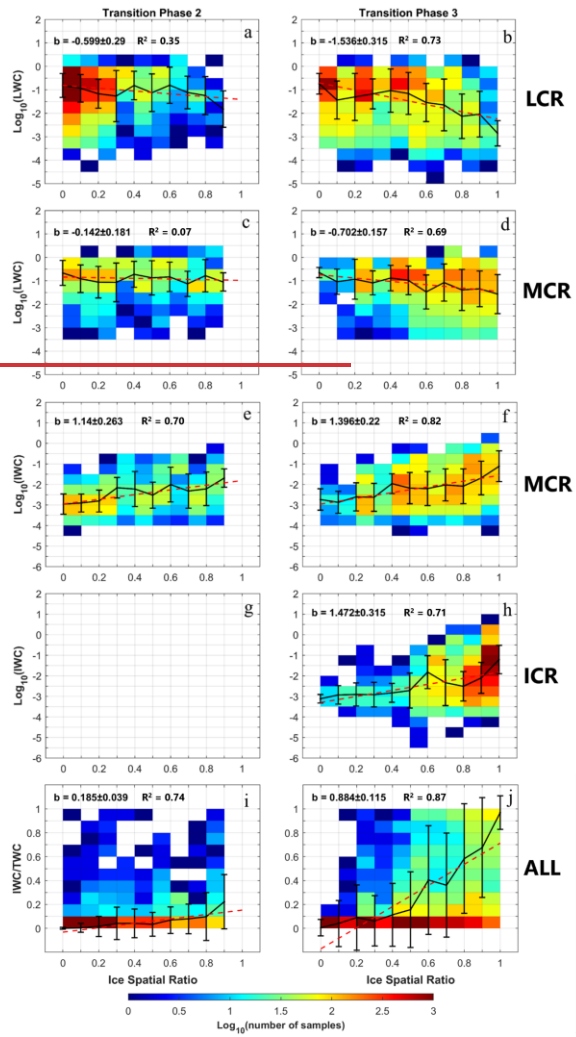
Figure 6. Similar to Figure 5, but separated into four temperature ranges.

Formatted: Left, Line spacing: single





930 **Figure 7.** Relationship between ice particle number fraction and mixed spatial ratio or ice spatial ratio, separated by the transition phases (phase 2 in column 1 and phase 3 in column 2), and by various cloud segments – (a, b) LCR, (c, d) MCR and (e, f) ICR. Average values for each ice spatial ratio bin are shown in black solid lines, with vertical bars representing standard deviations. Linear fit is shown in red dashed line. Average values of generating cells (time series obtained from 935 Wang et al. (2020)) are in purple/pink “X” markers. The slope value b, and its associated error standard deviation, are also shown along with and the ordinary R-squared value are shown in the legend.





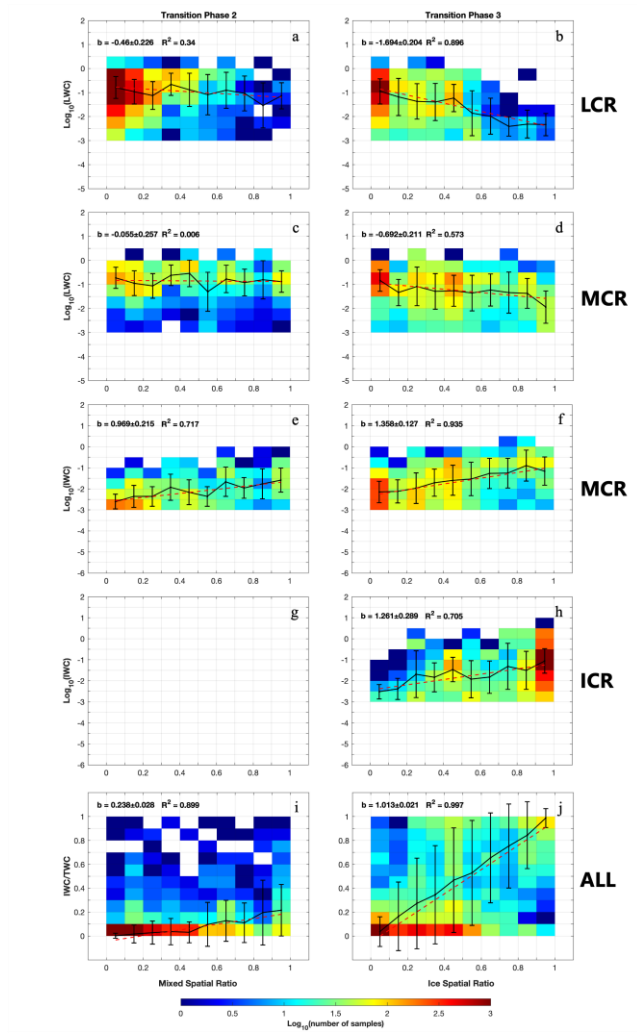


**Figure 8.** Similar to Figure 7, but showing (a-d) LWC, (e-h) IWC, and (i and j) ice mass fraction in relation to mixed spatial ratio for phase 2 and ice spatial ratio for phase 3, separated by the transition phases and cloud regions.

940

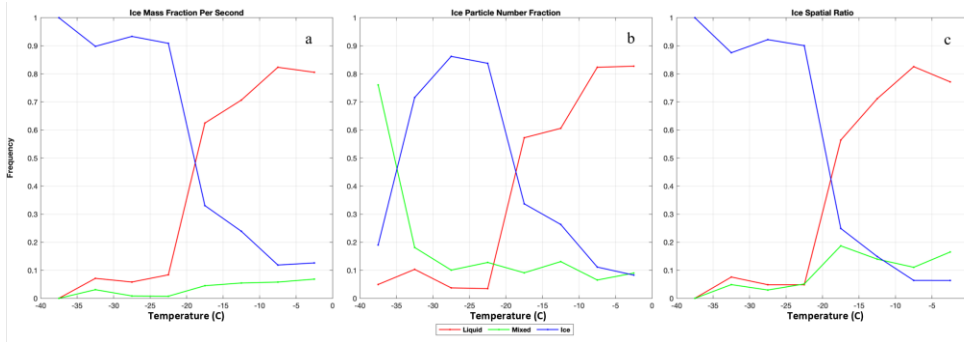


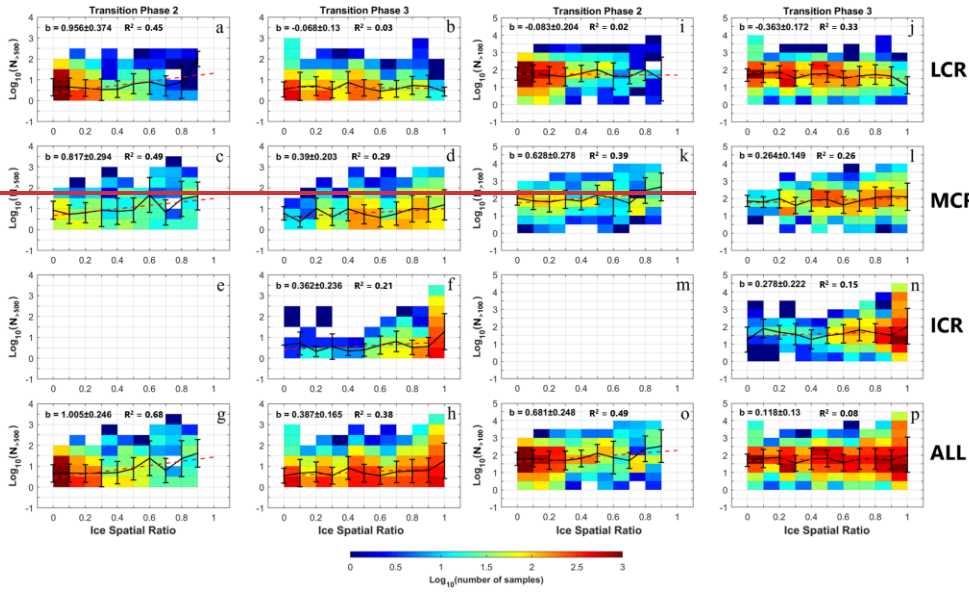
**Figure 9.** Cloud phase occurrence frequencies at various temperatures. Cloud phase identification methods are based on (a) ice mass fraction per second, (b) ice particle number fraction per second, and (c) ice spatial ratio calculated for individual consecutive TCR.

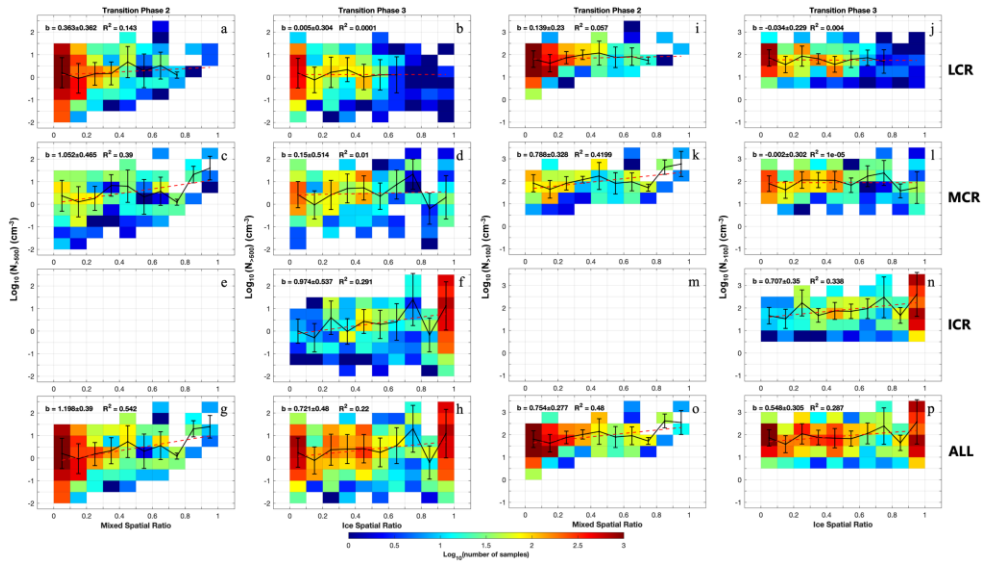
945

**Formatted:** English (United Kingdom), Do not check spelling or grammar

**Formatted:** Space After: 0 pt, Line spacing: single

Formatted: Justified, Line spacing: 1.5 lines





950

**Figure 109.** Similar to Figure 7, but showing logarithmic scale (a-h)  $N_{>500}$  and (i-p)  $N_{>100}$  in relation to mixed spatial ratio or ice spatial ratio, separated by the transition phases and cloud regions. The last row represents all cloud regions in a specific transition phase. The aerosol number concentrations represent the moving average values of every 50 seconds.

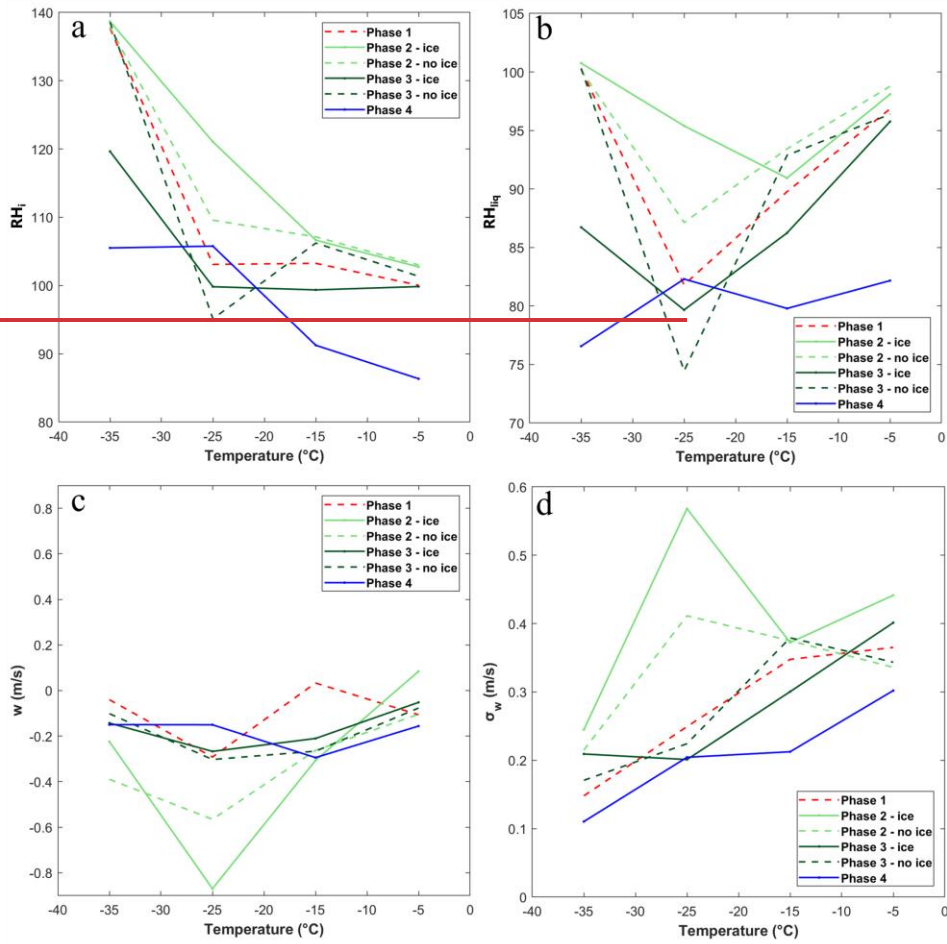


Figure 10. Distributions of (a)  $RH_i$ , (b)  $RH_{lig}$ , (c) vertical velocity ( $w$ ) and (d) standard deviation of vertical velocity ( $\sigma_w$ ) for various transition phases at different temperatures.

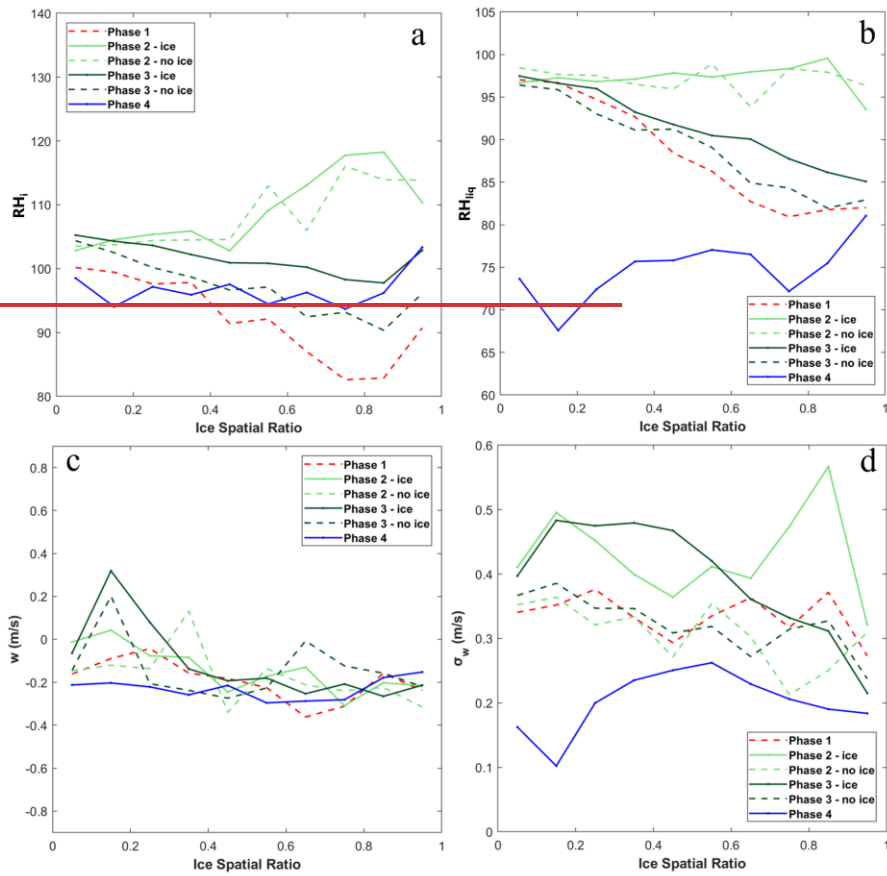


Figure 11. Similar to Figure 10, but in relation to various ice spatial ratios.

Formatted: Centered